M-type (22) Kalliope: A tiny Mercury

Marin Ferrais, L. Jorda, Pierre Vernazza, Benoit Carry, M. Broz, N. Rambaux, J. Hanus, G. Dudzinski, P. Bartczak, F. Vachier, et al.

Astronomy & Astrophysics manuscript no. output
March 29, 2022

M-type (22) Kalliope: A tiny Mercury ⋆,⋆⋆

M. Ferrais[1], L. Jorda[1], P. Vernazza[1], B. Carry[2], M. Brož[3], N. Rambaux[4], J. Hanuš[3], G. Dudziński[5], P. Bartczak[5], F. Vachier[4], E. Aristidi[2], P. Beck[6], F. Marchis[1,7], M. Marsset[8], M. Viikinkoski[9], R. Fetick[1,10], A. Drouard[1], T. Fusco[1,10], M. Birlan[4,11], E. Podlewska-Gaca[5,12], T. H. Burbine[13], M. D. Dyar[13], P. Bendjoya[2], Z. Benkhaldoun[14], J. Berthier[4], J. Castillo-Rogez[15], F. Cipriani[16], F. Colas[4], C. Dumas[17], J. Ďurech[3], S. Fauvaud[18], J. Grice[19], E. Jehin[20], †M. Kaasalainen[9], A. Kryszczynska[5], P. Lamy[21], H. Le Coroller[1], A. Marciniak[5], T. Michalowski[5], P. Michel[2], J.-L Prieur[22], V. Reddy[23], J.-P. Rivet[2], T. Santana-Ros[24,25], M. Scardia[26,2], P. Tanga[2], A. Vigan[1], O. Witasse[17], and B. Yang[27,28]

(Affiliations can be found after the references)

Received x-x-2022 / Accepted x-x-2022

ABSTRACT

Context. Asteroid (22) Kalliope is the second largest M-type asteroid in the main belt and is orbited by a satellite, Linus. Whereas the mass of Kalliope is already well constrained thanks to the presence of a moon, its volume is still poorly known, leading to uncertainties on its bulk density and internal structure.

Aims. We aim to refine the shape of (22) Kalliope and thus its diameter and bulk density, as well as the orbit of its moon to better constrain its mass, hence density and internal structure.

Methods. We acquired disk-resolved observations of (22) Kalliope using the VLT/SPHERE/ZIMPOL instrument to reconstruct its three-dimensional (3D) shape using three different modeling techniques. These images were also used together with new speckle observations at the C2PU/PISCO instrument as well as archival images from other large ground-based telescopes to refine the orbit of Linus.

Results. The volume of (22) Kalliope given by the shape models, corresponding to $D = 150 \pm 5$ km, and the mass constrained by its satellite's orbit yield a density of $\rho = 4.40 \pm 0.46$ g · cm^{-3}. This high density potentially makes (22) Kalliope the densest known small body in the Solar System. A macroporosity in the 10-25% range (as expected for this mass and size), implies a grain density in the 4.8–5.9 g · cm^{-3} range. Kalliope's high bulk density, along with its silicate-rich surface implied by its low radar albedo, implies a differentiated interior with metal contributing to most of the mass of the body.

Conclusions. Kalliope's high metal content (40–60%) along with its metal-poor mantle makes it the smallest known Mercury-like body. A large impact at the origin of the formation of the moon Linus is likely the cause of its high metal content and density.

Key words. minor planets, asteroids: individual: (22) Kalliope – methods: observational – techniques: high angular resolution

1. Introduction

Asteroid (22) Kalliope (hereafter Kalliope) is one of the largest M-type (metallic) asteroids in the main belt, along with (16) Psyche and (216) Kleopatra (Ferrais et al. 2020; Marchis et al. 2021). A satellite was discovered orbiting Kalliope in 2001 by Merline et al. (2001) and Margot & Brown (2001) using the Canada-France-Hawaii Telescope and the Keck II telescope on Mauna Kea, respectively. Initially designated S/2001 (22) 1, this satellite was afterward named "Linus".

The first detailed dynamical characterizations of the binary system were published shortly after in Merline et al. (2002) and Margot & Brown (2003). The latter notably determined an unexpectedly low density of 2.37 ± 0.4 g · cm^{-3} for an M-type object, when combining their mass measurements with the IRAS diameter of 181 km (Tedesco et al. 2004). They concluded that chondritic material is dominant in the composition of the interior of Kalliope, with a porosity reaching ∼30%, a value surprisingly high for such a large asteroid (Carry 2012).

The previous diameter estimates, however, show a large dispersion, ranging between 140 and 196 km (Usui et al. 2011; Marchis et al. 2008), with an average of 154±17 km (Drummond et al. 2021). In contrast, the determination of Linus' orbital parameters puts stringent constraints on the mass of Kalliope with a weighted average of $(7.89 \pm 0.09) \times 10^{18}$ kg (Merline et al. 2002; Margot & Brown 2003; Descamps et al. 2008; Marchis et al. 2008; Vachier et al. 2012). As a result, a bulk density of 4.1 ± 1.4 g · cm^{-3} can be derived from this exploration of the literature. However, most of the recently reported bulk density estimates are between 3.1 and 3.7 g · cm^{-3} (e.g., Carry 2012; Vachier et al. 2012; Hanuš et al. 2017; Drummond et al. 2021).

Kalliope's surface materials possess a high optical albedo ($\rho_v = 0.166 \pm 0.005$; Mainzer et al. 2019) as well as two absorption bands at 0.9 μm and 3 μm, as revealed by near-infrared spectroscopic observations (Hardersen et al. 2011; Rivkin et al. 2000; Usui et al. 2019). These two features suggest the presence of low-calcium pyroxene and hydrated minerals, respectively. Finally, Kalliope's low radar albedo of 0.18 ± 0.05 is not compatible with a metal-rich surface (Shepard et al. 2015). At this stage, a meteoritic analog for Kalliope is still to be determined.

We present here disk-resolved adaptive-optics images of Kalliope obtained as part of our ESO Large Program (PI: P. Vernazza; ID: 199.C-0074; Vernazza et al. 2021) with the

⋆ Based on observations made with ESO Telescopes at the Paranal Observatory under program ID 199.C-0074 (PI: P. Vernazza).

⋆⋆ The reduced images and the shape models are available at the CDS via anonymous ftp to http://cdsarc.u-strasbg.fr/ (130.79.128.5) or via http://cdsarc.u-strasbg.fr/viz-bin/qcat?J/A+A/xxx/Axxx

Article published by EDP Sciences, to be cited as https://doi.org/10.1051/0004-6361/202243200

VLT/SPHERE instrument. These new data allow Kalliope's three-dimensional (3D) shape to be reconstructed using three different algorithms (Sect. 3). The SPHERE images are also used to refine the orbit of the satellite by complementing them with new speckle observations of the Kalliope–Linus system and archival data (Sect. 4).

2. Observations and data reduction

2.1. High angular resolution imaging

Kalliope was observed at seven epochs between March and May 2018 and in June 2019 with the Zurich Imaging Polarimeter (ZIMPOL) of the SPHERE instrument mounted on the VLT (Beuzit et al. 2019). The images were reduced using the procedure described in Vernazza et al. (2018) and then deconvolved with the `Mistral` algorithm (Fusco et al. 2003; Mugnier et al. 2004), using a parametric point spread function (PSF, Fétick et al. 2019). The 35 images obtained are presented in Fig. B.1 and the observational circumstances are given in Table B.1. In 2018 only the south pole of Kalliope was visible, while Kalliope was close to an equator-on geometry during the 2019 apparition, allowing us to increase the surface covered by the SPHERE images to 84% (Fig. B.2). Therefore, this data set allowed us to reconstruct a 3D shape model with tight constraints on the asteroid's dimensions.

For the extraction of the positions of Linus, we added a compilation of archival data to the SPHERE images from other large ground-based telescopes equipped with adaptive optic (AO) instruments (Keck II, ESO/VLT and Gemini-North). The camera used at Keck II was the Near InfraRed Camera (NIRC2, van Dam et al. 2004; Wizinowich et al. 2000). At the VLT, it was the NAOS-CONICA camera (NACO, Lenzen et al. 2004; Rousset et al. 2003) and another SPHERE camera, the InfraRed Dual-band Imager and Spectrograph (IRDIS, Dohlen et al. 2008). Finally, images acquired at Gemini-North used the Near InfraRed Imager (NIRI, Hodapp et al. 2003). This allowed us to increase the number of measurements to 94, spanning 48 epochs over 17.5 years (2001-2019).

These images were reduced using interactive data language (IDL) routines following the standard procedures of bad pixel correction, sky subtraction, and flat-field correction (for details, see Carry et al. 2008). The reduced images were then further processed to remove the bright halo around Kalliope, thus enhancing the detectability of Linus. The procedure is described in detail in Pajuelo et al. (2018) and Carry et al. (2019).

2.2. Speckle measurements

We also observed Kalliope in December 2021 with the Pupil Interferometry Speckle camera and COronagraph (PISCO, Scardia et al. 2019) at the 1 m C2PU telescope in Calern, Observatoire de la Cote d'Azur (OCA) (Bendjoya et al. 2012). Observations were carried out during the nights of December 30 and 31, 2021. The conditions were optimal and Kalliope was visible during the full night, with a minimum zenith distance of 10°. Images were recorded in the whole visible domain (λ = 550 nm, $\Delta\lambda$ = 500 nm) with an exposure time of 100 ms. This value of the exposure time is very long for speckle data (which is usually around 5–20 ms to freeze the turbulence), but we benefited from good seeing conditions ($\simeq$ 1 arcsec). The Kalliope–Linus pair, with a visual magnitude $V \simeq 10$ and a magnitude difference $\Delta V > 3$, is a difficult target for a 1m telescope. We were able to make 19 speckle measurements of the Kalliope system during the two nights.

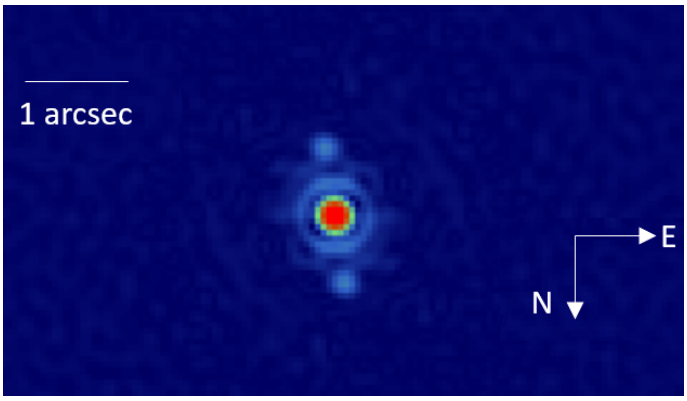

Fig. 1: Average autocorrelation from a speckle cube of Kalliope obtained on 2021-12-31T20:48:33 (UT). The measured angular separation is 678 ± 6 mas. The retained position angle value is 187.7 ± 0.3°, which corresponds to the small peak above the bright central peak.

For each measurement we recorded a cube of 14 000 short-exposure frames of both Kalliope and a nearby reference star (HD 47049). Data were processed via the classical Labeyrie's speckle interferometry technique (Labeyrie 1970), resulting in 2D visibilities and autocorrelations of specklegrams, as shown on Fig. 1. The autocorrelation function shows a central bright peak surrounded by two small symmetric spots. The position of these secondary peaks gives the relative astrometry of the pair (angular separation and position angle from the north), but there is a 180° ambiguity on the position angle, leading to two possible solutions. In the example shown in Fig. 1 the measured angular separation was 678 ± 6 mas and the position angle was 7.7 ± 0.3° or 187.7 ± 0.3°. The ambiguity was resolved by a comparison with the predicted position, and we retained the value 187.7 ± 0.3°.

We eventually obtained 19 astrometric measurements of Linus position respective to Kalliope, with a median uncertainty of 7 mas on the angular separation and 0.6° on the position angle. For the best image sequences it was also possible to derive the relative photometry of the couple from the visibility contrast. This makes C2PU the smallest telescope that directly measured the astrometry of a satellite of asteroids.

2.3. Optical light curves

We compiled 145 light curves from the DAMIT[1] and ALCDEF[2] databases, including 39 from the SuperWASP survey (Pollacco et al. 2006) for the period 2006–2008 (Grice et al. 2017). We complemented these data with observations from the 2016 and 2018 apparitions. Three light curves were obtained via the Gaia-Ground-based Observational Service for Asteroids (Gaia-GOSA)[3] project; five were acquired using the 60 cm TRAPPIST-North telescope (Jehin et al. 2011); and two by co-author S. Fauvaud with a C11 at f/3.2 and a SBIG ST402 M camera. In summary, we gathered a total of 155 light curves obtained between 1953 and 2018 that sample 18 different apparitions. Detailed information for each light curve is provided in Table B.2.

[1] https://astro.troja.mff.cuni.cz/projects/damit/
[2] www.alcdef.org
[3] www.gaiagosa.eu

3. Three-dimensional shape reconstruction

First, we derived the 3D shape model of Kalliope using the All-Data Asteroid Modeling algorithm (ADAM, Viikinkoski et al. 2015). We simultaneously fitted the sets of optical disk-integrated light curves and the 35 disk-resolved images from SPHERE. As in our previous works (e.g., Yang et al. 2020; Carry et al. 2021), we first derived a low-resolution shape solution with an initial estimate of the rotation state from Hanuš et al. (2017). Then, we increased the weights of the AO data with respect to the optical light curves and derived a shape solution with a higher resolution, leading to a volume-equivalent diameter $D_{\rm adam} = 153 \pm 3$ km.

Independently, we derived Kalliope's shape model with the Shaping Asteroid models using Genetic Evolution (SAGE) method, using the same data set of light curves and AO images as for the ADAM model. The method was developed for light curve inversion (Bartczak & Dudziński 2018), and later extended to include AO images as well (Dudziński et al. 2020). The weights for both types of observations are adjusted automatically during the modeling based on the best fits of individual observations. The AO images are treated as binary images, with value 0 set for the background, and 1 set for the pixels where the body is visible. Therefore, only the information about the body's silhouette is used. The SAGE model's axis of rotation is aligned with the axis of greatest moment of inertia, assuming a homogeneous density distribution. In addition, we calculated the model uncertainties (shape, pole, and volume) of the SAGE model using the method described in Bartczak & Dudziński (2019). The synthetic simulations of the nominal model's clones were compared with observations, and only those passing the test were selected (see Bartczak & Dudziński 2019 for details). This subset of clones was then scaled using AO images to derive size and volume uncertainties of the model. During this process, the resulting sizes are weighted by both the resolution and the aspect of AO images. The derived volume-equivalent diameter is $D_{\rm sage} = 147^{+8}_{-5}$ km.

Finally, we tried to further refine both the ADAM and SAGE models by using them as initial models for the Multi-resolution PhotoClinometry by Deformation (MPCD) method (Capanna et al. 2013; Jorda et al. 2016), following the procedure described in Ferrais et al. (2020). MPCD uses only the AO images to gradually deform the vertices of the 3D mesh in order to fit the synthetic images of the model to the observed images. The rotational parameters used (period and spin coordinates) were those determined by the initial methods, ADAM or SAGE. For the reflectance properties of Kalliope, we used the geometric albedo of 0.166 from Mainzer et al. (2016) and the Hapke parameters of the M-type asteroid (216) Kleopatra from Descamps et al. (2011). In both cases the initial models were only slightly modified by MPCD. The volume-equivalent diameter of the $\text{MPCD}_{\rm adam}$ model remained equal to 153 km, whereas for the $\text{MPCD}_{\rm sage}$ model it increased to 149 km. We report a final MPCD diameter by taking the average of the two models, leading to $D_{\rm mpcd} = 151 \pm 4$ km.

The appearances of the ADAM, SAGE, and the two MPCD shape models are shown in Fig. 2, where they are compared with the SPHERE data. Kalliope exhibits an elongated shape (a/b ~1.40, a/c ~1.72) featuring a large cavity (~70 km) at ~270° east longitude. This basin is responsible for the "pointy" appearance of Kalliope in most AO images. The physical properties of Kalliope are included in Table 1. From our three shape modeling methods we derive a volume-equivalent diameter $D = 150 \pm 5$ km, which yields a bulk density $\rho = 4.40 \pm 0.46$ g·cm^{-3} when combined with the mass $M = 7.78 \cdot 10^{18}$ kg derived from the orbital multipole model (see Sect. 4.2).

Table 1: Physical properties of (22) Kalliope based on the ADAM, SAGE, and MPCD shape modeling methods.

Parameter	ADAM	SAGE	MPCD
P (h)	4.148200(1)	4.148200(1)	4.148200(1)
λ (°)	195 ± 3	197^{+1}_{-0}	
β (°)	4 ± 3	3^{+2}_{-2}	
D (km)	153 ± 3	147^{+8}_{-5}	151 ± 4
a (km)	205 ± 3	194 ± 5	207 ± 7
b (km)	146 ± 3	141 ± 3	145 ± 5
c (km)	122 ± 3	114 ± 5	117 ± 7
a/b	1.40 ± 0.04	1.36 ± 0.05	1.43 ± 0.07
b/c	1.20 ± 0.04	1.24 ± 0.06	1.24 ± 0.09
a/c	1.68 ± 0.05	1.70 ± 0.09	1.77 ± 0.12
ρ (g·cm^{-3})	4.15 ± 0.28	4.68 ± 0.64	4.32 ± 0.37

Notes. The listed parameters are sidereal rotation period P; spin-axis ecliptic J2000 coordinates λ and β; volume-equivalent diameter D; dimensions along the major axis of the best-fit triaxial ellipsoids ($a > b > c$); their ratios a/b, b/c, and a/c; and bulk density ρ using the mass given by the orbital multipole model (Table 2). Uncertainties correspond to 1σ values.

The new diameter is significantly lower than the latest estimates of 161 ± 6 km (Hanuš et al. 2017) and 168 ± 3 km (Mainzer et al. 2019). While the value in Mainzer et al. (2019) is an indirect measurements depending on the thermal model and on the viewing geometry at the time of observation, in Hanuš et al. (2017) the same 3D shape modeling was performed with the ADAM method. However, only Keck/NIRC2 images were used, which have a spatial resolution that differs from that of the SPHERE images by a factor ~ 2.

4. Orbit of Linus

We measured 14 positions of Linus on the SPHERE/ZIMPOL images. We also measured 80 positions on the images we reprocessed from ESO/VLT, Keck, and Gemini archives. The positions of Kalliope and Linus were respectively measured by adjusting 2D Gaussian functions on the original image and on an image in which the Kalliope's halo was removed (Pajuelo et al. 2018). Finally, we measured 19 positions of Linus with PISCO/C2PU from speckle interferometry. We list these positions in Table B.3.

We complemented these 113 measurements with positions reported by other authors. Most of them were obtained with AO-fed cameras: 17 with the Starfire Optical Range (SOR, Drummond et al. 2021), 9 with PHARO at Palomar (Margot & Brown 2003), 9 with IRCAL at the Lick Observatory (Marchis et al. 2003), and 4 with the SCAM at Keck (Margot & Brown 2003). We also compiled 36 positions from speckle interferometry obtained with the BTA telescope (Sokova et al. 2014; Emelyanov et al. 2019) and one stellar occultation (Sôma et al. 2008). We thus have a data set of 188 positions of Linus spanning 7310 days.

4.1. Genoid

We used the Genoid algorithm (Vachier et al. 2012) to explore the dynamics of Linus, as we did for several other targets of our Large Program (Euphrosyne, Daphne, Sylvia, see Yang et al.

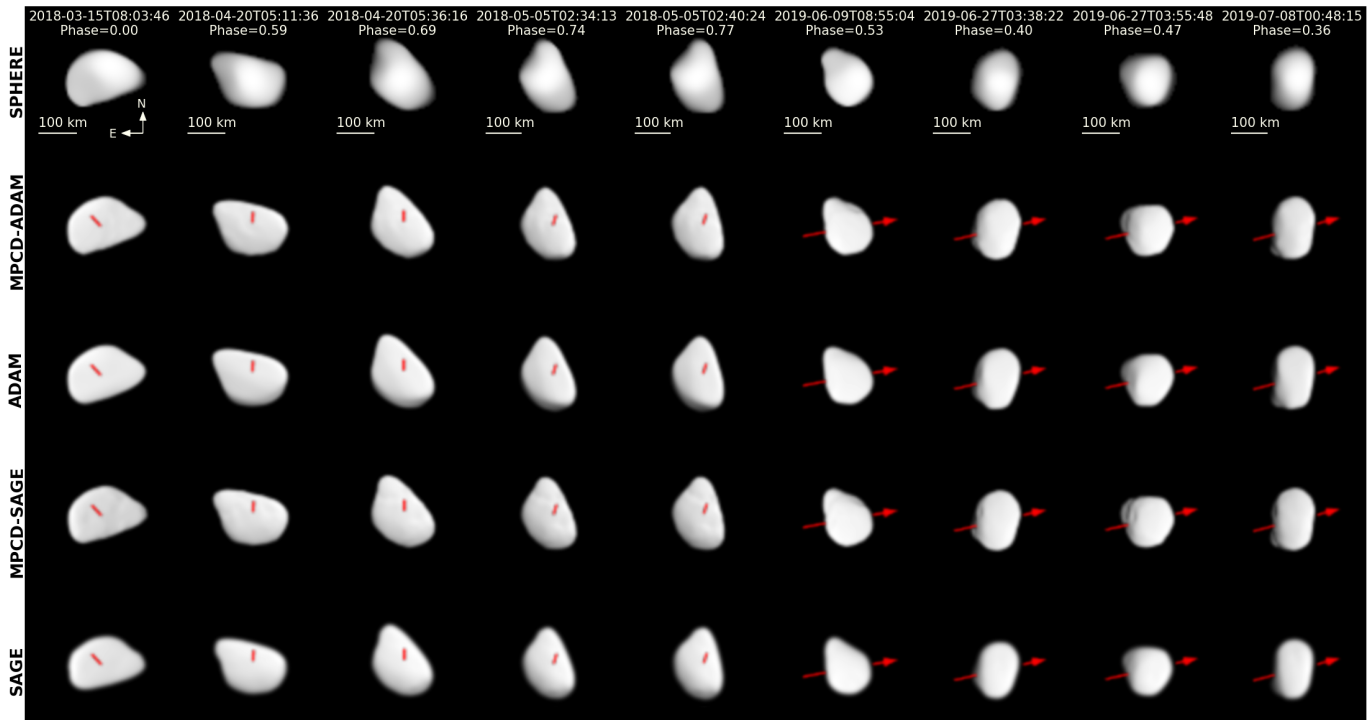

Fig. 2: Comparison between the deconvolved images of Kalliope (top row) and the corresponding synthetic images generated by the `OASIS` tool (Jorda et al. 2010) of the `ADAM` (third row), `SAGE` (fifth row), and the two associated `MPCD` shape models. The red arrows indicate the direction of the spin axis. The associated residuals are shown in Fig. B.3.

2020; Carry et al. 2019, 2021) As illustrated in the case of (216) Kleopatra (Brož et al. 2021), the topology of the parametric space is highly nontrivial to explore, with numerous local minima for the figure of merit (χ^2) in a high-dimensional space. Whereas gradient descent minimization is unlikely to find the absolute minimum, brute-force grids like Monte Carlo would be extremely CPU expensive. Markov chain Monte Carlo or genetic algorithms offer a compromise, with many trial solutions and denser grids closer to minima (Muinonen et al. 2016; Vachier et al. 2012).

`Genoid` explores the parameters (orbital period; eccentricity; inclination; longitude of the ascending node; argument of periapsis; time of passage to periapsis; and the lowest-order gravitational moment of the primary, the quadrupole J_2) in successive generations of orbital solutions. Each new generation is created by randomly merging the parameters of the best solutions from current generation. At each generation of solutions `Genoid` also uses a gradient descent to find the minimum closest to the best trial solution. The final orbital elements, mass of Kalliope, and coordinates of the orbital pole from fitting Keplerian motion are given in Table 2.

4.2. Multipole model

To describe the orbital motion of the moon more precisely, we also use the multipole numerical model of Brož et al. (2021)[4], previously used for (216) Kleopatra. This model accounts for the irregular shape of the central body, using its multipole expansion up to the order $\ell = 10$. We summarize the model in Appendix A.

For comparison, we first converged the Keplerian model ($\ell = 0$) and then re-converged all parameters for the multipole model ($\ell = 10$). These two results are shown in Fig. B.4. Interestingly, we were able to find orbital solutions for both models. Their $\chi^2_{\rm sky}$ values are comparable (202 vs 226) and relatively low, given the number of observations $N = 2 \cdot 158$ (counting the two sky-plane coordinates separately) and the number of free parameters $M = 10$. The uncertainties may be overestimated by a factor of approximately $\sqrt{(N-M)/\chi^2} \doteq 1.16$.

On the contrary, the models exhibit an important difference. The best-fit pole is (ECJ2000 longitude λ, latitude β) $\lambda = 195.6°$ and $\beta = +2.2°$, while the nominal pole according to the ADAM model is $\lambda_{\rm adam} = 195.0°$ and $\beta_{\rm adam} = 3.3°$. The explanation is that the multipole model is very sensitive; even a very small inclination of the orbit with respect to the equator of the central body would lead to observable precession in the longitude of node, $\dot{\Omega}_1$. This is not observed in astrometry and the model must adapt to this (i.e., by tilting the pole). The osculating period P_1 must also be adapted; it is longer by a factor of approximately 1.002 compared to the Keplerian model. Nevertheless, the additional precession results in the same $\dot{\lambda}_1 \equiv \dot{M}_1 + \dot{\omega}_1 + \dot{\Omega}_1$ with λ_1 the true longitude, M_1 the mean anomaly, ω_1 the argument of the pericenter, and Ω_1 the longitude of node.

We can actually take advantage of this. If we constrain the pole by the orbit, assuming it is exactly equatorial, we remove the shape ↔ pole degeneracy and the shape on its own should be significantly more precise. We checked that it is indeed possible to modify the shape, so that the pole is given by the best-fit pole. The residuals expressed as $\chi^2_{\rm ao}$ decreased from 460 to 448 (see Fig. B.5). We conclude that it is useful to account for the uncertainty of the pole when fitting the orbit(s) of the moon(s). The best-fit parameters for the three dynamical models are given in Table 2.

[4] `http://sirrah.troja.mff.cuni.cz/~mira/xitau/`

Table 2: Best-fit parameters for the `Genoid` model (Sect. 4.1) and the three dynamical models described in Sect. 4.2: Keplerian; multipole; multipole with fixed spin-axis pole.

		`Genoid`		Keplerian	multipole	fixed-pole	
var.	unit	val.	σ	val.	val.	val.	σ
m_1	10^{18} kg	7.72	0.61	7.75	7.78	7.80	0.26
m_2	10^{16} kg	0	–	0	4.72	4.71	3.96
P	day	3.595678	0.00002	3.595758	3.604302	3.604280	0.008544
e		0.002	$^{+0.012}_{-0.002}$	0.005	0.005	0.005	0.010
i	deg	93.9	2.6	87.356	88.104	86.232	1.0
a	km	1080	28				
Ω	deg	285.5	1.8				
ω	deg	154	20				
t_p	JD	2452215.18338	0.20374				
Ω_1	deg			15.8	15.9	15.5	1.0
ϖ_1	deg			327	326	327	10
λ_1	deg			206.3	206.3	206.0	1.0
$\lambda_{\rm pole}$	deg	195.8	1.5	–	195.6	195.1	1.0
$\beta_{\rm pole}$	deg	2.3	2.8	–	2.2	3.3	1.0
RMS	mas	8.1					
$\chi^2_{\rm sky}$				202	226	278	
$\chi^2_{\rm ao}$				453	460	448	

Notes. For the `Genoid` method, the orbital elements of Linus are expressed in EQJ2000. For the multipole method they are osculating for the epoch T_0 = 2454047.326750 JD and expressed in the standard stellar reference frame. If the orbit lies in the equatorial plane of body 1, they fulfill $i = 90° - b_{\rm pole}$, $\Omega = 180° + l_{\rm pole}$. m_1 denotes the mass of body 1 (i.e., Kalliope), m_2 body 2 (moon), P the orbital period of the orbit, e eccentricity, i inclination, a semi-major axis, Ω longitude of the ascending node, ω argument of pericenter, t_p time of pericenter, Ω_1 longitude of node, ϖ_1 longitude of pericenter, λ_1 true longitude, $\lambda_{\rm pole}$ ecliptic longitude of Kalliope's rotation pole, $\beta_{\rm pole}$ ecliptic latitude, RMS of residuals for the 113 measurements given in Table B.3, $\chi^2_{\rm sky}$ and $\chi^2_{\rm ao}$ are defined in App. A.

5. Discussion

5.1. Bulk composition and density

The smaller diameter determined here implies a much higher bulk density than previously estimated with a nominal value higher than recent estimates of the density of the metal-rich asteroid (16) Psyche: 4.20 ± 0.60 g·cm^{-3} (Ferrais et al. 2020) and 3.88 ± 0.25 g·cm^{-3} (Siltala & Granvik 2021). This means that Kalliope could be the densest known small body in the Solar System. Furthermore, given its smaller size with respect to Psyche (the second densest known small body in the Solar System), it is very likely that Kalliope is intrinsically more metal rich than Psyche since macroporosity is known to increase on average with decreasing size (e.g., Carry 2012). Assuming a porosity in the 10–25% range for Kalliope (as expected, following Carry 2012 and Vernazza et al. 2021) implies a density of its building blocks as high as 4.8-5.9 g·cm^{-3}. This density range excludes a number of possible meteoritic analogs, including iron, stony-iron (mesosiderites, pallasites), and CH chondrites (Consolmagno & Britt 1998; Britt & Consolmagno 2003). Neither stony-iron meteorites nor CH chondrites provide a satisfactory match to Kalliope's visible and near-infrared spectrum. What is sure at this stage is that Kalliope's surface is metal poor given its low radar albedo (Shepard et al. 2015). This likely suggests a very metal-rich interior to match the effective density of its building blocks (see above). Assuming a 10–25% macroporosity range and respectively density values for iron and silicates of 8 g·cm^{-3} and 3 g·cm^{-3}, we estimate the metal content of Kalliope to be in the 40–60% range. Such high metal content along with a metal-poor surface is reminiscent of the planet Mercury.

5.2. Internal structure

The fact that solutions exist for both Keplerian and multipole models means that the $J_2 \equiv -C_{20}$ value is not well constrained and we cannot determine whether the body is differentiated or not. It would be necessary to have a truly inclined (or eccentric) orbit to measure the precession directly, as $\dot{\Omega}_1$ (or $\dot{\varpi}_1$).

Nevertheless, some physical limits do exist. Assuming a spherical iron core surrounded by an irregular silicate mantle (densities 8 and 3 g·cm^{-3}), it is necessary to adjust the core–mantle boundary so that the total mass corresponds to the orbital solution (i.e., $7.78 \cdot 10^{18}$ kg), and the resulting $J_2 = 0.1166$. The shape is simply too irregular to have J_2 lower than this value (see also Fig. 3). However, Kalliope's high bulk density along with its silicate-rich surface, as implied by its low radar albedo (Shepard et al. 2015), still suggests that its interior is differentiated with a metallic core contributing to most of the mass of the body.

Similar arguments to those made above apply to the internal structure of (87) Sylvia, for which we recently reported differentiation, notably based on a null J_2 determined dynamically (Carry et al. 2021). However, we have now found acceptable orbital solutions for the nominal values of $J_2 = 0.1723$, corresponding to a homogeneous interior. In this case the density is low, 1.378 g·cm^{-3}. The lower limit of J_2 is probably 0.1521, obtained for a three-layer (core, mantle, crust) differentiated body with densities 1.788, 1.578, and 1.218 g·cm^{-3}, respectively. So, we do not exclude the possibility of differentiation, but the argument is softened because homogeneity is still not excluded.

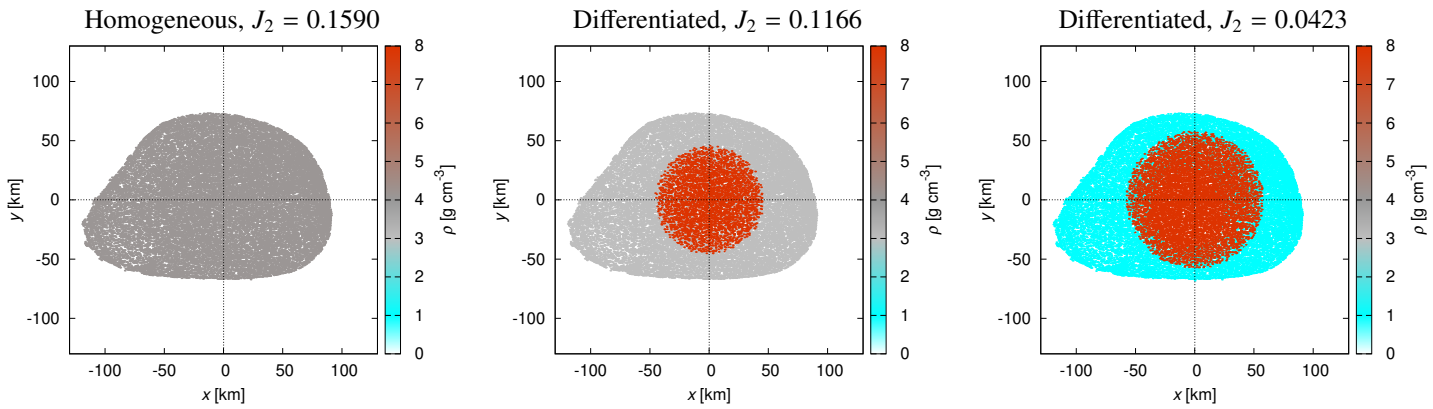

Fig. 3: Density profiles needed to obtain various J_2 values. The ADAM shape is used with fixed total mass $m_1 = 7.78 \cdot 10^{18}$ kg. Left: Homogeneous body with $\rho = 4.11$ g $\cdot$ cm^{-3}, and nominal $J_2 = 0.1590$. Middle: Differentiated body with iron core + silicate mantle ($\rho = 8$ and 3 g $\cdot$ cm^{-3}), and slightly lower $J_2 = 0.1166$; the core is spherical ($R \doteq 46$ km) and the mantle irregular. Right: Extreme example with iron core + icy mantle ($\rho = 8$ and 1 g $\cdot$ cm^{-3}), and $J_2 = 0.0423$ (not realistic, however). The body is always plotted as a section with $z < 0$ to see its interior.

5.3. Formation of Linus

Several observations point to a large impact as the origin of the formation of Kalliope's moon Linus: (i) a similar surface composition, as implied by component-resolved near-infrared spectra (Laver et al. 2009); (ii) a large cavity present in Kalliope's (Sect. 3); (iii) a recently identified family (to be discussed in a forthcoming paper; Brož et al. in prep.); (iv) Kalliope's high metal content and density. Similarly to the case of Mercury (Benz et al. 1988), collisional stripping of a proto-Kalliope could have resulted in a significant loss of its silicate mantle, explaining its unusually high density as well as the creation of a large moon and a family. Kalliope's high metal content (40–60% in volume) similar to that of Mercury (~60%, Wardinski et al. 2019) and metal-poor mantle makes it the smallest known Mercury-like body.

5.4. Dynamics of the system

The homogeneous processing of the data set presented in Sect. 4 allowed us to compute refined orbital elements of Linus, resulting in a RMS of residuals with the `Genoid` model of 8.1 mas over 20 years, significantly lower than previous works: 15 mas (Vachier et al. 2012) and 14 mas (Drummond et al. 2021). This makes it possible to compute the orbit of Linus with an accuracy of typically 7 mas over a similar period in the future. This will greatly help in the prediction of future stellar occultations.

Recently, Emelyanov et al. (2019) announced the detection of the precession of the orbit of Linus around the spin axis of Kalliope, in contradiction with the present results and several previous studies (Marchis et al. 2008; Vachier et al. 2012; Drummond et al. 2021). Emelyanov et al. 2019 compiled all observation of Linus from 2001 to 2018, divided them into six groups of observations close in time, fitted Keplerian orbits to each group, and determined their poles. The poles of these orbits indicated a polar wandering, featuring an unusual change from a prograde to a retrograde motion. However, the residuals between their predicted and measured positions are quite high (4 to 120 mas) and the authors indicate that the pole coordinates are heavily dependent on the choice of the observations used in each fit. We use a larger data set (188 vs 121 observations) that includes theirs, and over a longer time span (7310 vs 5986 days). The data set is different, however, because we homogeneously reprocessed all the data from VLT, Keck, and Gemini.

The nodal precession $\dot{\Omega}$ must take place given the irregular shape of the body, but because of the almost-precisely determined equatorial orbit of Linus it is not directly observable. Together with the orbital motion, which occurs at the rate of n, and the pericenter precession $\dot{\omega}$, it does contribute to the total rate of the true longitude (i.e., $\dot{\lambda} \equiv n + \dot{\omega} + \dot{\Omega}$). The only way to directly observe the effect of nonzero J_2, would be a detection of short-term perturbations, which occur at half of the rotational period of Kalliope. A continuous series of AO observations, and astrometry with respect to a suitable (stable) comparison star would be needed for this purpose.

6. Conclusion

We acquired disk-resolved observations of (22) Kalliope using the VLT/SPHERE/ZIMPOL instrument to reconstruct its 3D shape and determine its density. The volume of (22) Kalliope given by the shape models, corresponding to $D = 150 \pm 5$ km, and the mass constrained by the orbit of its satellite yield a density of $\rho = 4.40 \pm 0.46$ g $\cdot$ cm^{-3}. This high density potentially makes (22) Kalliope the densest known small body in the Solar System. A macroporosity in the 10–25% range (as expected for such a mass and size) implies a grain density in the 4.8-5.9 g $\cdot$ cm^{-3} range. Kalliope's high bulk density, along with its silicate-rich surface implied by its low radar albedo, implies a differentiated interior with metal contributing to most of the mass of the body. A giant impact stripping a large portion of Kalliope's mantle would help to explain the formation of a large moon such as Linus as well as Kalliope's high density and metal content but metal-poor surface, which is reminiscent of Mercury.

Acknowledgements. Based on observations collected at the European Organisation for Astronomical Research in the Southern Hemisphere under ESO programme 199.C-0074 (PI: P. Vernazza). P. Vernazza, A. Drouard, M. Ferrais and B. Carry were supported by CNRS/INSU/PNP. The research of JH has been supported by the Czech Science Foundation through grant 20-08218S and by Charles University Research program No. UNCE/SCI/023. M.B. was supported by the Czech Science Foundation, grant 21-11058S. F.M. is supported by the National Science Foundation under Grant No. 1743015. TRAPPIST is a project funded by the Belgian Fonds (National) de la Recherche Scientifique (F.R.S.-FNRS) under grant PDR T.0120.21. TRAPPIST-North is a project funded by the University of Liège, in collaboration with the Cadi Ayyad University of Marrakech (Morocco). E.J. is F.R.S.-FNRS Senior Research Associate. The work

of TSR was carried out through grant APOSTD/2019/046 by Generalitat Valenciana (Spain). This work was supported by the MINECO (Spanish Ministry of Economy) through grant RTI2018-095076-B-C21 (MINECO/FEDER, UE).

References

Ahmad, I. I. 1954, ApJ, 120, 551
Bartczak, P. & Dudziński, G. 2018, MNRAS, 473, 5050
Bartczak, P. & Dudziński, G. 2019, MNRAS, 485, 2431
Barucci, M. A. & Dipaoloantonio, A. 1983, A&A, 117, 1
Bendjoya, P., Abe, L., Rivet, J. P., et al. 2012, in SF2A-2012: Proceedings of the Annual meeting of the French Society of Astronomy and Astrophysics, ed. S. Boissier, P. de Laverny, N. Nardetto, R. Samadi, D. Valls-Gabaud, & H. Wozniak, 643–648
Benz, W., Slattery, W. L., & Cameron, A. G. W. 1988, Icarus, 74, 516
Beuzit, J. L., Vigan, A., Mouillet, D., et al. 2019, A&A, 631, A155
Britt, D. T. & Consolmagno, G. J. 2003, Meteoritics and Planetary Science, 38, 1161
Brož, M., Marchis, F., Jorda, L., et al. 2021, A&A, 653, A56
Brož, M., Ševeček, P., Vernazza, P., & Ferrais, M. in prep., A&A
Capanna, C., Gesquière, G., Jorda, L., Lamy, P., & Vibert, D. 2013, The Visual Computer, 29, 825
Carry, B. 2012, Planet. Space Sci., 73, 98
Carry, B., Dumas, C., Fulchignoni, M., et al. 2008, A&A, 478, 235
Carry, B., Vachier, F., Berthier, J., et al. 2019, A&A, 623, A132
Carry, B., Vernazza, P., Vachier, F., et al. 2021, A&A, 650, A129
Consolmagno, G. J. & Britt, D. T. 1998, Meteoritics and Planetary Science, 33, 1231
Descamps, P., Marchis, F., Berthier, J., et al. 2011, Icarus, 211, 1022
Descamps, P., Marchis, F., Pollock, J., et al. 2008, Icarus, 196, 578
di Martino, M. & Cacciatori, S. 1984, Icarus, 60, 75
Dohlen, K., Langlois, M., Saisse, M., et al. 2008, in Society of Photo-Optical Instrumentation Engineers (SPIE) Conference Series, Vol. 7014, Ground-based and Airborne Instrumentation for Astronomy II, ed. I. S. McLean & M. M. Casali, 70143L
Dotto, E., Barucci, M. A., Fulchignoni, M., et al. 1992, A&AS, 95, 195
Drummond, J. D., Merline, W. J., Carry, B., et al. 2021, Icarus, 358, 114275
Dudziński, G., Podlewska-Gaca, E., Bartczak, P., et al. 2020, MNRAS, 499, 4545
Emelyanov, N. V., Safonov, B. S., & Kupreeva, C. D. 2019, MNRAS, 489, 3953
Ferrais, M., Vernazza, P., Jorda, L., et al. 2020, A&A, 638, L15
Fétick, R. J., Jorda, L., Vernazza, P., et al. 2019, A&A, 623, A6
Fusco, T., Mugnier, L. M., Conan, J.-M., et al. 2003, in Proc. SPIE, Vol. 4839, Adaptive Optical System Technologies II, ed. P. L. Wizinowich & D. Bonaccini, 1065–1075
Gehrels, T. & Owings, D. 1962, ApJ, 135, 906
Grice, J., Snodgrass, C., Green, S. F., Parley, N. R., & Carry, B. 2017, in Asteroids, Comets, and Meteors: ACM 2017
Hanuš, J., Ďurech, J., Oszkiewicz, D. A., et al. 2016, A&A, 586, A108
Hanuš, J., Viikinkoski, M., Marchis, F., et al. 2017, A&A, 601, A114
Hardersen, P. S., Cloutis, E. A., Reddy, V., Mothé-Diniz, T., & Emery, J. P. 2011, Meteoritics and Planetary Science, 46, 1910
Hodapp, K. W., Jensen, J. B., Irwin, E. M., et al. 2003, PASP, 115, 1388
Jehin, E., Gillon, M., Queloz, D., et al. 2011, The Messenger, 145, 2
Jorda, L., Gaskell, R., Capanna, C., et al. 2016, Icarus, 277, 257
Jorda, L., Spjuth, S., Keller, H. U., Lamy, P., & Llebaria, A. 2010, Society of Photo-Optical Instrumentation Engineers (SPIE) Conference Series, Vol. 7533, OASIS: a simulator to prepare and interpret remote imaging of solar system bodies, 753311
Labeyrie, A. 1970, Astron. Astroph., 6, 85
Laver, C., de Pater, I., Marchis, F., Ádámkovics, M., & Wong, M. H. 2009, Icarus, 204, 574
Lenzen, R., Close, L., Brandner, W., Biller, B., & Hartung, M. 2004, in Society of Photo-Optical Instrumentation Engineers (SPIE) Conference Series, Vol. 5492, Ground-based Instrumentation for Astronomy, ed. A. F. M. Moorwood & M. Iye, 970–977
Lupishko, D. F., Belskaia, I. N., Tupieva, F. A., & Chernova, G. P. 1982, Astronomicheskii Vestnik, 16, 101
Lupishko, D. F., Tupieva, F. A., Velichko, F. P., & Bel'Skaya, I. N. 1989, Bjull. Inst. Astrofizikii, 80, 13
Mainzer, A. K., Bauer, J. M., Cutri, R. M., et al. 2016, NASA Planetary Data System, 247
Mainzer, A. K., Bauer, J. M., Cutri, R. M., et al. 2019, NASA Planetary Data System
Marchis, F., Descamps, P., Baek, M., et al. 2008, Icarus, 196, 97
Marchis, F., Descamps, P., Hestroffer, D., et al. 2003, Icarus, 165, 112
Marchis, F., Jorda, L., Vernazza, P., et al. 2021, A&A, 653, A57
Margot, J. L. & Brown, M. E. 2001, IAU Circ., 7703, 3
Margot, J. L. & Brown, M. E. 2003, Science, 300, 1939
Melillo, F. J. 1987, Minor Planet Bulletin, 14, 42
Merline, W. J., Menard, F., Close, L., et al. 2001, IAU Circ., 7703, 2
Merline, W. J., Tamblyn, P. M., Dumas, C., et al. 2002, IAU Circ., 7980
Michalowski, T. & Velichko, F. P. 1990, Acta Astron., 40, 321
Mugnier, L. M., Fusco, T., & Conan, J.-M. 2004, JOSA A, 21, 1841
Muinonen, K., Fedorets, G., Pentikäinen, H., et al. 2016, Planet. Space Sci., 123, 95
Pajuelo, M., Carry, B., Vachier, F., et al. 2018, Icarus, 309, 134
Pollacco, D. L., Skillen, I., Collier Cameron, A., et al. 2006, PASP, 118, 1407
Rivkin, A. S., Howell, E. S., Lebofsky, L. A., Clark, B. E., & Britt, D. T. 2000, Icarus, 145, 351
Rousset, G., Lacombe, F., Puget, P., et al. 2003, in Society of Photo-Optical Instrumentation Engineers (SPIE) Conference Series, Vol. 4839, Adaptive Optical System Technologies II, ed. P. L. Wizinowich & D. Bonaccini, 140–149
Scaltriti, F., Zappala, V., & Stanzel, R. 1978, Icarus, 34, 93
Scardia, M., Rivet, J.-P., Prieur, J.-L., et al. 2019, Astronomische Nachrichten, 340, 771
Shepard, M. K., Taylor, P. A., Nolan, M. C., et al. 2015, Icarus, 245, 38
Si, H. 2006, Available at http://wias-berlin.de/software/tetgen/
Siltala, L. & Granvik, M. 2021, ApJ, 909, L14
Sokova, I. A., Sokov, E. N., Roschina, E. A., et al. 2014, Icarus, 236, 157
Sôma, M., Hayamizu, T., Miyashita, K., Setoguchi, T., & Hirose, T. 2008, in A Giant Step: from Milli- to Micro-arcsecond Astrometry, ed. W. J. Jin, I. Platais, & M. A. C. Perryman, Vol. 248, 130–131
Surdej, J., Pospieszalska-Surdej, A., Michalowski, T., & Schober, H. J. 1986, A&A, 170, 167
Tedesco, E. F., Noah, P. V., Noah, M., & Price, S. D. 2004, NASA Planetary Data System, 12
Usui, F., Hasegawa, S., Ootsubo, T., & Onaka, T. 2019, PASJ, 71, 1
Usui, F., Kuroda, D., Müller, T. G., et al. 2011, PASJ, 63, 1117
Vachier, F., Berthier, J., & Marchis, F. 2012, A&A, 543, A68
van Dam, M. A., Le Mignant, D., & Macintosh, B. A. 2004, Applied Optics IP, 43, 5458
Vernazza, P., Brož, M., Drouard, A., et al. 2018, A&A, 618, A154
Vernazza, P., Ferrais, M., Jorda, L., et al. 2021, A&A, 654, A56
Viikinkoski, M., Kaasalainen, M., & Ďurech, J. 2015, A&A, 576, A8
Wardinski, I., Langlais, B., & Thébault, E. 2019, Journal of Geophysical Research: Planets, 124, 2178
Warner, B. D. 2007, Minor Planet Bulletin, 34, 72
Weidenschilling, S. J., Chapman, C. R., Davis, D. R., Greenberg, R., & Levy, D. H. 1990, Icarus, 86, 402
Weidenschilling, S. J., Chapman, C. R., Davis, D. R., et al. 1987, Icarus, 70, 191
Wizinowich, P. L., Acton, D. S., Lai, O., et al. 2000, in Society of Photo-Optical Instrumentation Engineers (SPIE) Conference Series, Vol. 4007, Adaptive Optical Systems Technology, ed. P. L. Wizinowich, 2–13
Yang, B., Hanuš, J., Carry, B., et al. 2020, A&A, 641, A80
Zappala, V. & van Houten-Groeneveld, I. 1979, Icarus, 40, 289
Zhou, X. H., Yang, X. Y., & Wu, Z. X. 1982, Acta Astronomica Sinica, 23, 349

[1] Aix Marseille Université, CNRS, CNES, Laboratoire d'Astrophysique de Marseille, Marseille, France
e-mail: marin.ferrais@lam.fr
[2] Université Côte d'Azur, Observatoire de la Côte d'Azur, CNRS, Laboratoire Lagrange, France
[3] Charles University, Faculty of Mathematics and Physics, Institute of Astronomy, V Holešovičkách 2, CZ-18000, Prague 8, Czech Republic
[4] IMCCE, CNRS, Observatoire de Paris, PSL Université, Sorbonne Université, Paris, France
[5] Astronomical Observatory Institute, Faculty of Physics, Adam Mickiewicz University, Słoneczna 36, 60-286 Poznań, Poland
[6] Institut de Planetologie et d'Astrophysique de Grenoble, UGA-CNRS, France; Institut Universitaire de France, Paris, France
[7] SETI Institute, Carl Sagan Center, 189 Bernado Avenue, Mountain View CA 94043, USA
[8] Department of Earth, Atmospheric and Planetary Sciences, MIT, 77 Massachusetts Avenue, Cambridge, MA 02139, USA
[9] Mathematics and Statistics, Tampere University, 33720 Tampere, Finland
[10] ONERA The French Aerospace Laboratory, Châtillon, France
[11] Astronomical Institute of the Romanian Academy, 5-Cuţitul de Argint, 040557 Bucharest, Romania
[12] Institute of Physics, University of Szczecin, Wielkopolska 15, 70-453 Szczecin, Poland
[13] Department of Astronomy, Mount Holyoke College, South Hadley, MA 01075 USA
[14] Oukaimeden Observatory, High Energy Physics and Astrophysics Laboratory, Cadi Ayyad University, Marrakech, Morocco
[15] Jet Propulsion Laboratory, California Institute of Technology, 4800 Oak Grove Drive, Pasadena, CA 91109, USA
[16] European Space Agency, ESTEC - Scientific Support Office, Keplerlaan 1, Noordwijk 2200 AG, The Netherlands
[17] TMT Observatory, 100 W. Walnut Street, Suite 300, Pasadena, CA 91124, USA
[18] Observatoire du Bois de Bardon, 16110 Taponnat, France
[19] Open University, School of Physical Sciences, The Open University, MK7 6AA, UK
[20] Space sciences, Technologies and Astrophysics Research Institute, Université de Liège, Allée du 6 Août 17, 4000 Liège, Belgium
[21] Laboratoire Atmosphères, Milieux et Observations Spatiales, CNRS & Université de Versailles Saint-Quentin-en-Yvelines, Guyancourt, France
[22] Université de Toulouse – UPS-OMP – IRAP, Toulouse, France
[23] Lunar and Planetary Laboratory, University of Arizona, 1629 E University Boulevard, Tucson, AZ 85721-0092, USA
[24] Departamento de Fisica, Ingeniería de Sistemas y Teoría de la Señal, Universidad de Alicante, Alicante, Spain
[25] Institut de Ciències del Cosmos (ICCUB), Universitat de Barcelona (IEEC-UB), Martí Franquès 1, E08028 Barcelona, Spain
[26] INAF – Osservatorio Astronomico di Brera, Merate, Italy
[27] European Southern Observatory (ESO), Alonso de Cordova 3107, 1900 Casilla Vitacura, Santiago, Chile
[28] Núcleo de Astronomía, Facultad de Ingeniería y Ciencias, Universidad Diego Portales

Appendix A: Multipole model

We describe here the multipole expansion model of Kalliope's shape. Specifically, the potential is expressed as

$$U = -\frac{GM}{r}\sum_{\ell=0}^{10}\left(\frac{R}{r}\right)^{\ell}\sum_{m=0}^{\ell}P_{\ell m}(\cos\theta)[C_{\ell m}\cos(m\phi)+S_{\ell m}\sin(m\phi)]\,, \tag{A.1}$$

$$C_{\ell m} = \frac{2}{MR^{\ell}}\frac{(\ell-m)!}{(\ell+m)!}\int_V \rho\,|\boldsymbol{r}|^{\ell}P_{\ell m}(\cos\theta)\cos(m\phi)\,\mathrm{d}V\,, \tag{A.2}$$

$$S_{\ell m} = \frac{2}{MR^{\ell}}\frac{(\ell-m)!}{(\ell+m)!}\int_V \rho\,|\boldsymbol{r}|^{\ell}P_{\ell m}(\cos\theta)\sin(m\phi)\,\mathrm{d}V\,, \tag{A.3}$$

where M denotes the mass; R the reference radius; r, θ, ϕ the body-frozen spherical coordinates; $P_{\ell m}$ the Legendre polynomials; and ρ the density. The derivatives of U were presented in Brož et al. (2021). Moreover, our model includes the external tides of the Sun. The coefficients computed for the `ADAM` surface mesh and homogeneous interior are listed in Table B.4. Alternately, we also computed them for differentiated interior $\rho(|\boldsymbol{r}|)$. The volume was discretized with the Tetgen program (Si 2006) to 50809 tetrahedral elements. The discretisation error was estimated for an equivalent sphere with irregular (isotropic) mesh, discretized to 63620 elements. The absolute error is about 10^{-4} in C_{20}; other coefficients have relative errors of less than 10^{-2}, which is surely smaller than the uncertainties of the surface mesh.

The difference between the Keplerian and the multipole models, and both astrometric observations and adaptive-optics silhouettes, is expressed as

$$\chi^2 = w_{\mathrm{sky}}\chi^2_{\mathrm{sky}} + w_{\mathrm{ao}}\chi^2_{\mathrm{ao}}\,, \tag{A.4}$$

$$\chi^2_{\mathrm{sky}} = \sum_{i=1}^{N_{\mathrm{sky}}}\frac{(u'_i-u_i)^2+(u'_i-v_i)^2}{\sigma^2_{\mathrm{sky}\,i}}\,, \tag{A.5}$$

$$\chi^2_{\mathrm{ao}} = \sum_{i=1}^{N_{\mathrm{ao}}}\sum_{k=1}^{360}\frac{(u'_{ik}-u_{ik})^2+(v'_{ik}-v_{ik})^2}{\sigma^2_{\mathrm{ao}\,i}}\,, \tag{A.6}$$

where u, v denote the observed sky-plane coordinates; u', v' the corresponding synthetic coordinates; σ the observational uncertainties, and w the corresponding weights. The χ^2_{ao} term is used for regularization, to prevent incompatible spin-axis pole orientation. We usually assume $w_{\mathrm{sky}} = 1$, $w_{\mathrm{ao}} = 0.3$ for this purpose. The values of the best-fit parameters are summarized in Table 2.

Appendix B: Additional figures and tables

Table B.1: Observational circumstances for each VLT/SPHERE disk-resolved image obtained by the ZIMPOL camera with the N_R photometric filter.

Date	UT	Exp (s)	Airmass	α (°)	D_{a} ($''$)
2018-03-15	08:03:46	360	1.32	8.3	0.108
2018-03-15	08:09:57	360	1.34	8.3	0.108
2018-03-15	08:16:07	360	1.35	8.3	0.108
2018-03-15	08:22:17	360	1.38	8.3	0.108
2018-03-15	08:28:25	360	1.40	8.3	0.108
2018-04-20	05:11:36	360	1.34	8.5	0.107
2018-04-20	05:17:47	360	1.36	8.5	0.107
2018-04-20	05:23:57	360	1.38	8.5	0.107
2018-04-20	05:30:06	360	1.40	8.5	0.107
2018-04-20	05:36:16	360	1.42	8.5	0.107
2018-05-04	23:30:43	360	1.83	12.3	0.102
2018-05-04	23:36:53	360	1.78	12.3	0.102
2018-05-04	23:43:04	360	1.73	12.3	0.102
2018-05-04	23:49:14	360	1.68	12.3	0.102
2018-05-04	23:55:24	360	1.64	12.3	0.102
2018-05-05	02:34:13	360	1.23	12.4	0.102
2018-05-05	02:40:24	360	1.23	12.4	0.102
2018-05-05	02:46:35	360	1.23	12.4	0.102
2018-05-05	02:52:44	360	1.23	12.4	0.102
2018-05-05	02:58:53	360	1.24	12.4	0.102
2019-06-09	08:50:43	252	1.53	2.8	0.106
2019-06-09	08:55:04	252	1.56	2.8	0.106
2019-06-09	08:59:26	252	1.59	2.8	0.106
2019-06-09	09:03:47	252	1.62	2.8	0.106
2019-06-09	09:08:08	252	1.66	2.8	0.106
2019-06-27	03:38:22	252	1.00	4.9	0.106
2019-06-27	03:42:43	252	1.00	4.9	0.106
2019-06-27	03:47:05	252	1.00	4.9	0.106
2019-06-27	03:51:26	252	1.00	4.9	0.106
2019-06-27	03:55:48	252	1.00	4.9	0.106
2019-07-08	00:30:49	252	1.17	8.4	0.104
2019-07-08	00:35:12	252	1.16	8.4	0.104
2019-07-08	00:39:34	252	1.15	8.5	0.104
2019-07-08	00:43:54	252	1.14	8.5	0.104
2019-07-08	00:48:15	252	1.13	8.5	0.104

Notes. For each image the table gives the epoch, exposure time, airmass, phase angle α, and angular diameter D_{a} of Kalliope as seen from the Earth.

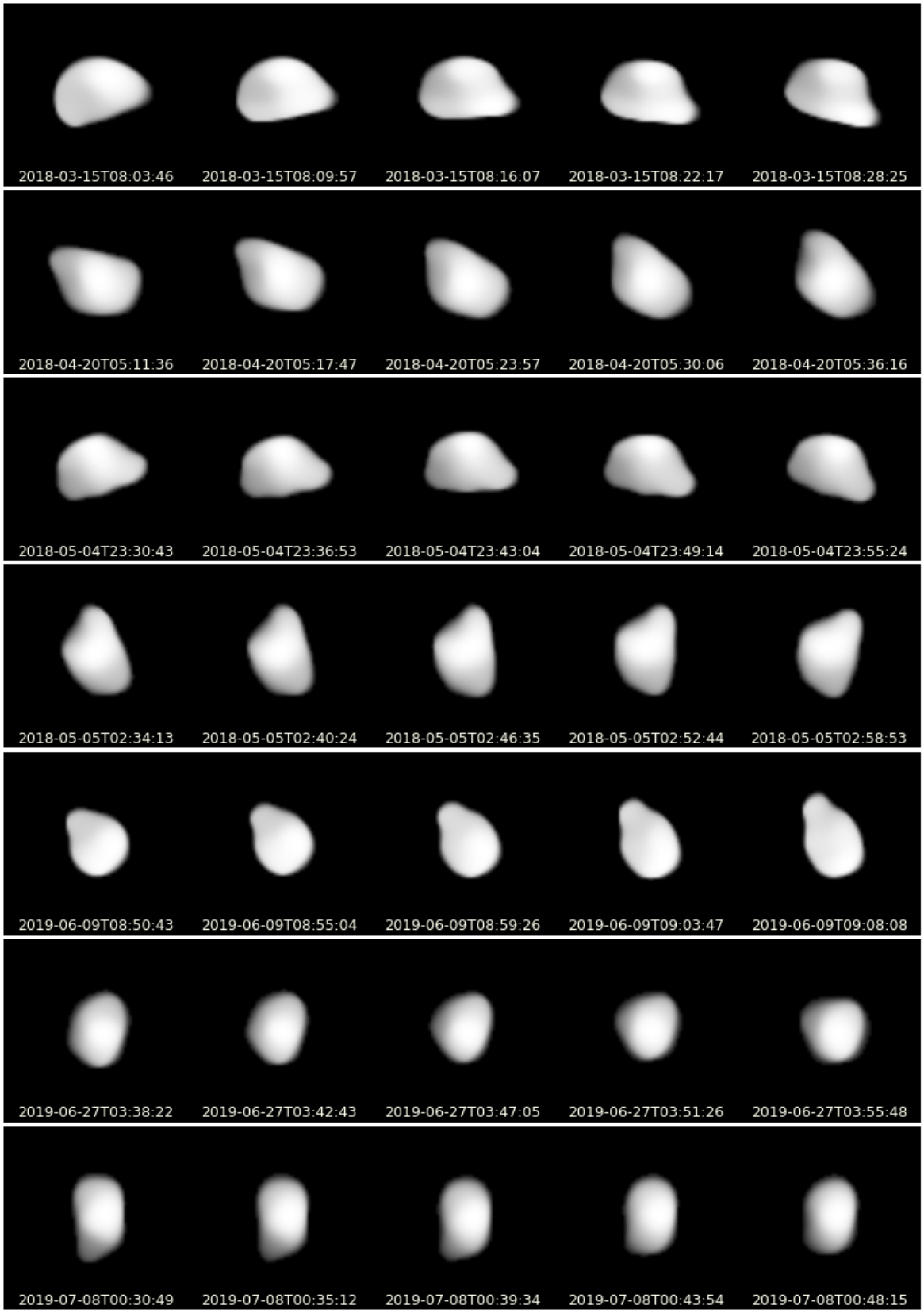

Fig. B.1: VLT/SPHERE/ZIMPOL images of Kalliope used for our shape reconstruction. The 35 images were obtained at seven different epochs between March 2018 and July 2019, and were deconvolved with the `Mistral` algorithm.

Table B.2: Optical disk-integrated light curves used for `ADAM` shape modeling.

N	Epoch	N_p	Δ (AU)	r (AU)	φ (°)	Filter	Reference
1	1953-02-13.5	12	1.94	2.88	7.3	V	Ahmad (1954)
2	1953-02-15.4	70	1.94	2.88	7.1	V	Ahmad (1954)
3	1958-02-24.3	84	1.96	2.90	6.9	V	Gehrels & Owings (1962)
4	1965-09-04.9	46	2.13	2.96	13.0	C	Zappala & van Houten-Groeneveld (1979)
5	1974-06-12.9	57	2.26	3.21	7.6	C	Zappala & van Houten-Groeneveld (1979)
6	1976-10-18.0	167	1.81	2.61	15.8	V	Scaltriti et al. (1978)
7	1976-10-32.0	138	1.70	2.61	10.9	V	Scaltriti et al. (1978)
8	1976-11-14.9	89	1.64	2.61	5.0	V	Scaltriti et al. (1978)
9	1976-11-16.8	112	1.63	2.61	4.1	V	Scaltriti et al. (1978)
10	1976-11-20.0	273	1.63	2.61	2.7	V	Scaltriti et al. (1978)
11	1976-11-26.0	212	1.62	2.61	0.5	V	Scaltriti et al. (1978)
12	1976-11-27.8	157	1.62	2.61	1.1	V	Scaltriti et al. (1978)
13	1976-12-08.8	117	1.65	2.61	6.1	V	Scaltriti et al. (1978)
14	1979-05-22.9	6	2.19	3.21	0.9	V	Lupishko et al. (1982)
15	1979-05-25.9	50	2.19	3.21	0.4	V	Lupishko et al. (1982)
16	1979-05-26.8	33	2.19	3.21	0.7	V	Lupishko et al. (1982)
17	1979-05-29.8	68	2.20	3.21	1.7	V	Lupishko et al. (1982)
18	1979-06-02.8	6	2.20	3.21	3.2	V	Lupishko et al. (1982)
19	1979-06-26.7	6	2.33	3.20	11.0	V	Lupishko et al. (1982)
20	1981-08-06.4	9	2.76	2.63	21.5	C	Weidenschilling et al. (1987)
21	1981-11-03.9	119	1.72	2.61	11.6	V	Lupishko et al. (1989)
22	1981-11-04.2	6	1.72	2.61	11.4	V	Weidenschilling et al. (1987)
23	1981-11-05.3	12	1.71	2.61	11.0	V	Weidenschilling et al. (1987)
24	1981-11-06.3	6	1.70	2.61	10.6	V	Weidenschilling et al. (1987)
25	1981-11-30.8	87	1.63	2.61	0.4	V	Barucci & Dipaoloantonio (1983)
26	1981-12-01.6	57	1.63	2.62	0.7	V	Zhou et al. (1982)
27	1982-01-09.3	16	1.85	2.62	16.0	V	Weidenschilling et al. (1987)
28	1982-02-17.3	21	2.34	2.64	21.8	V	Weidenschilling et al. (1987)
29	1982-12-16.3	13	2.73	2.90	19.9	V	Weidenschilling et al. (1987)
30	1982-12-17.3	10	2.72	2.90	19.8	V	Weidenschilling et al. (1987)
31	1983-02-18.4	8	2.08	2.96	10.3	V	Weidenschilling et al. (1987)
32	1983-02-20.3	17	2.07	2.96	9.8	V	Weidenschilling et al. (1987)
33	1983-03-08.1	116	2.03	2.98	6.7	V	di Martino & Cacciatori (1984)
34	1983-03-28.4	19	2.08	3.00	8.7	V	Weidenschilling et al. (1987)
35	1983-03-29.2	18	2.08	3.00	8.9	V	Weidenschilling et al. (1987)
36	1983-05-22.4	11	2.64	3.05	18.8	V	Weidenschilling et al. (1987)
37	1983-05-23.3	10	2.65	3.05	18.9	V	Weidenschilling et al. (1987)
38	1983-05-24.3	7	2.67	3.05	18.9	V	Weidenschilling et al. (1987)
39	1983-07-02.2	10	3.21	3.08	18.4	V	Weidenschilling et al. (1987)
40	1984-01-15.4	6	3.65	3.19	14.6	V	Weidenschilling et al. (1987)
41	1984-01-16.4	8	3.64	3.19	14.7	V	Weidenschilling et al. (1987)
42	1984-04-08.2	14	2.52	3.20	14.7	V	Weidenschilling et al. (1987)
43	1984-04-09.3	23	2.50	3.20	14.6	V	Weidenschilling et al. (1987)
44	1984-05-08.4	15	2.24	3.20	6.8	V	Weidenschilling et al. (1987)
45	1984-05-09.2	16	2.24	3.20	6.5	V	Weidenschilling et al. (1987)
46	1984-06-10.4	22	2.21	3.20	5.2	V	Weidenschilling et al. (1987)
47	1984-07-05.3	9	2.38	3.20	12.7	V	Weidenschilling et al. (1987)
48	1985-10-25.3	5	2.41	2.85	19.6	V	Weidenschilling et al. (1987)
49	1985-10-26.3	7	2.42	2.85	19.7	V	Weidenschilling et al. (1987)
50	1985-06-25.3	9	2.31	2.97	17.0	V	Weidenschilling et al. (1987)
51	1985-06-27.3	10	2.29	2.97	16.7	V	Weidenschilling et al. (1987)
52	1985-08-17.2	66	1.95	2.92	6.9	V	Surdej et al. (1986)
53	1985-10-21.3	12	2.37	2.85	19.2	V	Weidenschilling et al. (1987)
54	1985-10-23.3	6	2.39	2.85	19.5	V	Weidenschilling et al. (1987)
55	1986-11-26.1	108	1.65	2.63	3.7	V	Dotto et al. (1992)
56	1986-12-05.2	14	1.64	2.63	1.0	C	Melillo (1987)
57	1986-12-08.9	49	1.65	2.63	2.5	V	Michalowski & Velichko (1990)
58	1987-01-07.9	91	1.82	2.64	14.4	V	Dotto et al. (1992)
59	1987-01-23.8	176	1.99	2.64	18.5	V	Dotto et al. (1992)

Table B.2: continued

N	Epoch	N_p	Δ (AU)	r (AU)	φ (°)	Filter	Reference
60	1988-04-25.2	20	2.29	3.03	14.9	V	Weidenschilling et al. (1990)
61	1988-04-26.3	6	2.30	3.03	15.1	V	Weidenschilling et al. (1990)
62	2004-06-06.0	75	2.18	3.20	1.1	C	Hanuš et al. (2016)
63	2004-06-07.0	42	2.18	3.20	1.1	C	Hanuš et al. (2016)
64	2004-06-10.0	38	2.18	3.20	1.8	C	Hanuš et al. (2016)
65	2004-06-10.0	48	2.18	3.20	1.8	C	Hanuš et al. (2016)
66	2004-06-11.0	58	2.19	3.20	2.1	C	Hanuš et al. (2016)
67	2004-06-11.0	67	2.19	3.20	2.1	C	Hanuš et al. (2016)
68	2004-06-14.0	37	2.19	3.20	3.1	C	Hanuš et al. (2016)
69	2004-06-17.0	37	2.20	3.19	4.1	C	Hanuš et al. (2016)
70	2004-06-18.0	22	2.20	3.19	4.4	C	Hanuš et al. (2016)
71	2004-06-19.0	129	2.20	3.19	4.8	C	Hanuš et al. (2016)
72	2006-11-10	54	1.83	2.62	15.6	C	Grice et al. (2017)
73	2006-11-03.6	125	1.90	2.62	17.7	C	Hanuš et al. (2016)
74	2006-11-05.6	70	1.88	2.62	17.2	C	Hanuš et al. (2016)
75	2006-11-09.6	82	1.84	2.62	16.1	C	Hanuš et al. (2016)
76	2006-11-12.6	119	1.82	2.62	15.2	C	Hanuš et al. (2016)
77	2006-12-30.9	110	1.68	2.64	6.1	C	Hanuš et al. (2016)
78	2006-11-10	57	1.83	2.62	15.6	C	Grice et al. (2017)
79	2006-11-30	40	1.69	2.63	8.6	C	Grice et al. (2017)
80	2006-12-13	35	1.66	2.63	3.8	C	Grice et al. (2017)
81	2006-12-29	68	1.68	2.64	5.8	C	Grice et al. (2017)
82	2006-12-29	89	1.68	2.64	5.8	C	Grice et al. (2017)
83	2006-12-30	54	1.68	2.64	6.2	C	Grice et al. (2017)
84	2007-01-22	39	1.84	2.65	14.4	C	Grice et al. (2017)
85	2007-01-22	40	1.84	2.65	14.4	C	Grice et al. (2017)
86	2007-02-03	69	1.96	2.66	17.6	C	Grice et al. (2017)
87	2007-02-25.2	216	2.23	2.67	20.9	R	Warner (2007)
88	2007-02-27.2	139	2.25	2.67	21.0	R	Warner (2007)
89	2007-02-28.9	65	2.28	2.68	21.2	C	Hanuš et al. (2016)
90	2007-03-02.2	188	2.29	2.68	21.3	R	Warner (2007)
91	2007-03-04.2	176	2.32	2.68	21.4	R	Warner (2007)
92	2007-03-05.2	162	2.34	2.68	21.4	R	Warner (2007)
93	2007-02-03	72	1.96	2.66	17.6	C	Grice et al. (2017)
94	2007-03-05.9	179	2.35	2.68	21.5	C	Hanuš et al. (2016)
95	2007-03-08.2	160	2.38	2.68	21.6	R	Warner (2007)
96	2007-03-09.2	176	2.39	2.68	21.6	R	Warner (2007)
97	2007-03-10.0	108	2.40	2.68	21.6	C	Hanuš et al. (2016)
98	2007-03-12.9	292	2.44	2.68	21.7	C	Hanuš et al. (2016)
99	2007-03-13.2	131	2.45	2.68	21.7	R	Warner (2007)
100	2007-03-14.2	84	2.46	2.69	21.7	R	Warner (2007)
101	2007-03-15.9	303	2.48	2.69	21.7	C	Hanuš et al. (2016)
102	2007-03-17.9	53	2.51	2.69	21.7	C	Hanuš et al. (2016)
103	2007-03-20.9	234	2.55	2.69	21.7	C	Hanuš et al. (2016)
104	2007-02-08	47	2.02	2.66	18.6	C	Grice et al. (2017)
105	2007-05-15.2	41	3.26	2.74	16.7	V	V. Reddy
106	2007-05-17.2	33	3.28	2.74	16.4	V	V. Reddy
107	2007-05-18.2	15	3.29	2.74	16.3	V	V. Reddy
108	2007-02-09	47	2.03	2.66	18.8	C	Grice et al. (2017)
109	2007-02-09	49	2.03	2.66	18.8	C	Grice et al. (2017)
110	2007-02-10	39	2.05	2.66	19.0	C	Grice et al. (2017)
111	2007-02-10	44	2.05	2.66	19.0	C	Grice et al. (2017)
112	2007-01-14	43	1.77	2.65	11.8	C	Grice et al. (2017)
113	2007-01-21	41	1.83	2.65	14.1	C	Grice et al. (2017)
114	2008-02-23.4	95	2.21	3.02	12.5	V	V. Reddy
115	2008-02-04	67	2.38	3.00	16.4	C	Grice et al. (2017)
116	2008-03-04	47	2.14	3.03	9.7	C	Grice et al. (2017)
117	2008-03-07	54	2.12	3.03	8.9	C	Grice et al. (2017)
118	2008-03-10	66	2.11	3.04	8.1	C	Grice et al. (2017)
119	2008-03-18	103	2.09	3.04	6.4	C	Grice et al. (2017)

Table B.2: continued

N	Epoch	N_p	Δ (AU)	r (AU)	φ (°)	Filter	Reference
120	2008-03-18	107	2.09	3.04	6.4	C	Grice et al. (2017)
121	2008-03-29	47	2.09	3.05	5.8	C	Grice et al. (2017)
122	2008-04-01	52	2.09	3.05	6.1	C	Grice et al. (2017)
123	2008-04-13	70	2.14	3.06	8.7	C	Grice et al. (2017)
124	2008-04-14	86	2.14	3.07	8.9	C	Grice et al. (2017)
125	2008-04-20	85	2.18	3.07	10.5	C	Grice et al. (2017)
126	2008-04-21	51	2.19	3.07	10.7	C	Grice et al. (2017)
127	2008-04-21	105	2.19	3.07	10.7	C	Grice et al. (2017)
128	2008-04-22	70	2.20	3.07	11.0	C	Grice et al. (2017)
129	2008-04-23	64	2.21	3.07	11.2	C	Grice et al. (2017)
130	2008-04-24	64	2.21	3.07	11.5	C	Grice et al. (2017)
131	2008-04-28	74	2.25	3.08	12.5	C	Grice et al. (2017)
132	2008-04-29	86	2.26	3.08	12.7	C	Grice et al. (2017)
133	2008-05-04	60	2.30	3.08	13.9	C	Grice et al. (2017)
134	2008-05-05	32	2.31	3.08	14.1	C	Grice et al. (2017)
135	2008-05-06	43	2.33	3.08	14.3	C	Grice et al. (2017)
136	2012-01-15.9	41	1.77	2.67	10.6	C	Hanuš et al. (2016)
137	2012-01-15.9	41	1.77	2.67	10.6	C	Hanuš et al. (2016)
138	2012-01-16.9	77	1.77	2.67	10.9	C	Hanuš et al. (2016)
139	2012-01-16.9	77	1.77	2.67	10.9	C	Hanuš et al. (2016)
140	2012-02-07.9	351	1.98	2.68	17.3	C	Hanuš et al. (2016)
141	2012-02-08.0	90	1.98	2.68	17.4	R	Hanuš et al. (2016)
142	2012-02-08.0	92	1.98	2.68	17.4	C	Hanuš et al. (2016)
143	2012-02-08.0	111	1.98	2.68	17.4	C	Hanuš et al. (2016)
144	2012-02-08.9	210	1.99	2.68	17.6	C	Hanuš et al. (2016)
145	2012-02-17.0	208	2.09	2.69	19.1	C	Hanuš et al. (2016)
146	2016-11-17.2	39	1.87	2.64	16.0	C	GaiaGosa
147	2016-11-18.2	41	1.86	2.65	15.7	C	GaiaGosa
148	2016-11-5.1	189	2.00	2.64	18.9	C	GaiaGosa
149	2018-3-9.2	335	2.17	3.06	10.0	R	TRAPPIST-North
150	2018-3-10.2	510	2.17	3.06	9.7	R	TRAPPIST-North
151	2018-3-11.0	62	2.16	3.06	9.5	R	TRAPPIST-North
152	2018-3-12.0	325	2.15	3.06	9.2	R	TRAPPIST-North
153	2018-3-14.0	159	2.14	3.06	8.6	R	TRAPPIST-North
154	2018-4-18.1	1112	2.15	3.09	7.9	R	S. Fauvaud
155	2018-4-19.1	1387	2.15	3.09	8.1	R	S. Fauvaud

Notes. For each light curve the table gives the epoch, the number of individual measurements N_p, the asteroid's distance to the Earth Δ and the Sun r, the phase angle φ, the photometric filter, and the reference. Gaia-GOSA (Gaia-Ground-based Observational Service for Asteroids, www.gaiagosa.eu).

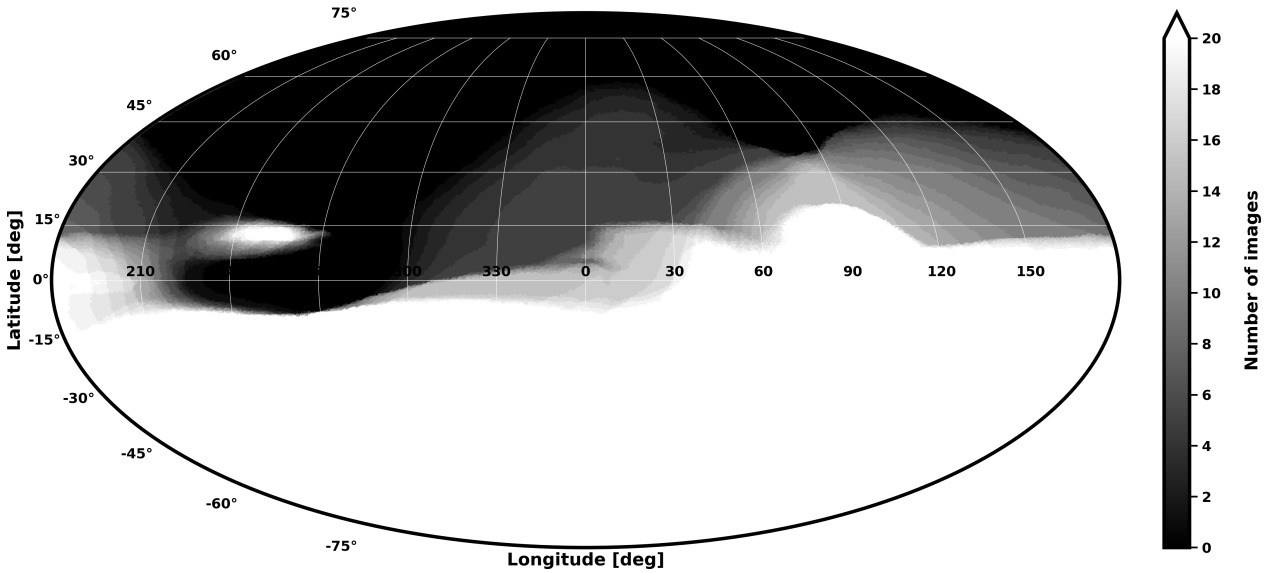

Fig. B.2: Coverage map of the surface of Kalliope. The number of times each facet of our ADAM shape model has been imaged by SPHERE/ZIMPOL is represented by different gray scales. The coverage of the southern hemisphere is much better than the northern, but 84% of the surface has been imaged at least once.

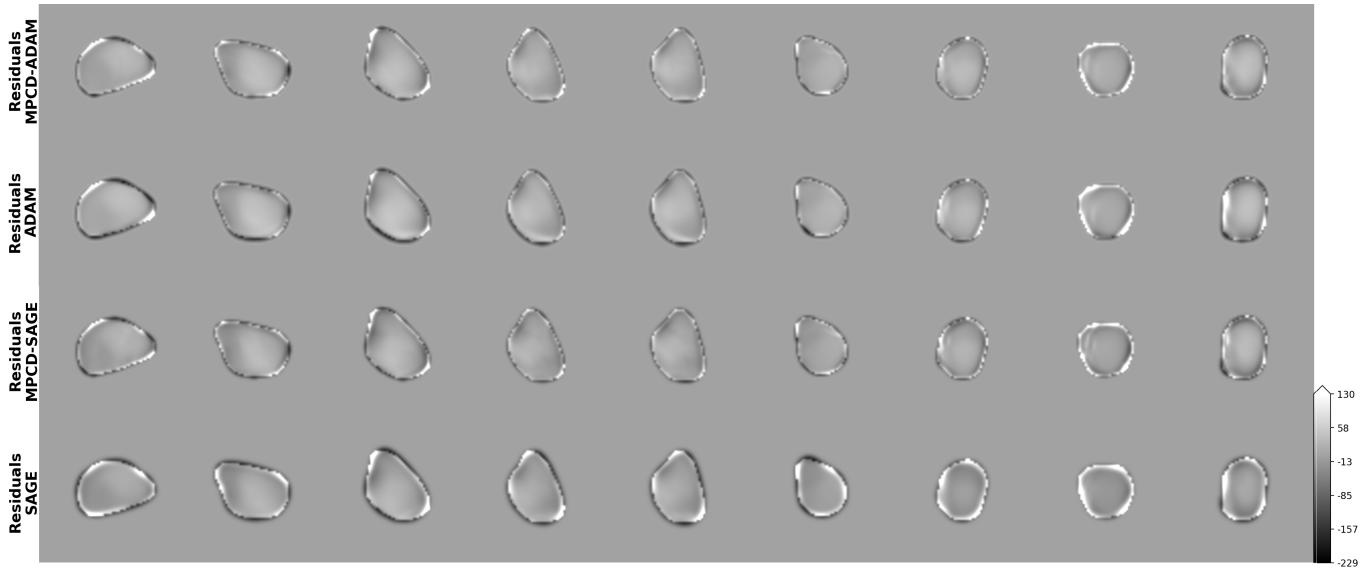

Fig. B.3: Residuals in units of instrumental noise between the observed SPHERE images and the corresponding synthetic images from the four shape models.

Table B.3: Astrometry of Kalliope's satellite Linus.

Date	UTC	Tel.	Cam.	Filter	X_o (mas)	Y_o (mas)	X_{o-c} (mas)	Y_{o-c} (mas)	σ (mas)	ΔM (mag)	δM (mag)
2001-12-27	10:10:54.83	Keck	NIRC2	Kp	-370.8	12.6	19.2	1.8	10.0	4.1	0.1
2001-12-27	10:14:02.43	Keck	NIRC2	Kp	-372.5	15.7	18.0	1.6	10.0	4.1	0.1
2001-12-27	10:23:07.08	Keck	NIRC2	H	-379.8	12.7	12.1	-11.0	10.0	4.8	1.2
2001-12-27	10:39:56.87	Keck	NIRC2	J	-385.3	49.9	9.1	8.4	10.0	4.4	0.1
2002-12-29	14:15:16.72	Keck	NIRC2	H	517.1	133.6	-6.6	3.8	10.0	5.8	0.2
2002-12-29	16:14:26.41	Keck	NIRC2	H	479.7	214.0	-20.6	12.9	10.0	6.6	1.2
2002-12-29	16:17:42.19	Keck	NIRC2	H	494.0	206.9	-5.5	3.9	10.0	5.1	0.1
2003-01-14	08:53:58.49	VLT	NACO	Ks	-526.3	249.6	-8.5	2.3	13.3	4.1	0.0
2003-01-14	09:00:18.55	VLT	NACO	H	-527.9	245.2	-8.1	1.8	13.3	4.1	0.0
2003-01-14	09:07:38.26	VLT	NACO	J	-529.9	240.0	-7.9	1.1	13.3	4.2	0.0
2003-02-14	08:22:00.84	VLT	NACO	H	645.7	165.1	0.5	-1.5	27.1	4.5	0.1
2003-06-05	08:01:52.16	Keck	NIRC2	Ks	449.3	-274.2	4.2	-7.6	10.0	4.3	0.0
2003-06-06	08:49:52.28	Keck	NIRC2	Ks	190.1	495.5	0.3	-7.5	10.0	4.1	0.0
2003-06-06	08:56:45.99	Keck	NIRC2	Ks	186.6	492.7	1.0	-11.5	10.0	3.5	0.1
2003-07-14	06:54:55.06	Keck	NIRC2	Kp	-29.1	-460.0	-0.1	-10.4	10.0	5.0	1.2
2003-07-15	00:58:12.96	VLT	NACO	H	427.0	-129.4	-2.1	4.0	27.1	4.0	0.1
2003-07-16	00:01:27.97	VLT	NACO	H	106.0	442.1	6.8	4.5	27.1	3.9	0.0
2004-03-03	10:08:24.53	VLT	NACO	H	-184.5	-350.9	-5.6	-5.2	13.3	4.7	0.1
2004-03-04	10:14:04.55	VLT	NACO	H	155.7	-250.9	-3.6	0.8	13.3	4.8	0.1
2004-06-04	09:45:47.30	Gemini	NIRI	Kp	-339.3	-8.8	-1.6	-2.1	21.9	3.6	0.0
2004-06-04	09:47:58.05	Gemini	NIRI	Kp	-332.6	-12.5	5.4	-4.0	21.9	3.1	0.1
2004-06-05	08:21:22.80	Gemini	NIRI	Kp	-62.5	-670.1	4.0	0.1	21.9	3.4	0.0
2004-06-05	11:03:50.60	Gemini	NIRI	Kp	0.4	-639.9	-2.3	6.0	21.9	3.8	0.0
2004-06-05	12:07:32.15	Gemini	NIRI	Kp	33.2	-630.0	3.3	-0.5	21.9	3.5	0.0
2004-06-05	13:22:56.93	Gemini	NIRI	Kp	65.5	-606.7	3.5	-1.4	21.9	3.9	0.0
2004-06-09	09:32:15.35	Gemini	NIRI	Kp	197.5	-436.0	-7.1	-5.6	21.9	3.9	1.2
2004-06-28	02:20:45.88	VLT	NACO	Ks	377.5	347.2	-2.8	6.9	13.3	4.0	0.0
2004-07-03	09:52:52.63	Keck	NIRC2	Kp	-393.8	-253.4	-1.9	2.6	10.0	4.3	0.0
2004-07-03	09:54:23.50	Keck	NIRC2	Kp	-395.7	-253.2	-3.9	3.9	10.0	4.4	0.1
2004-07-04	08:19:04.08	Keck	NIRC2	Kp	74.0	-561.7	-1.8	5.3	10.0	4.2	0.0
2004-07-04	08:28:54.13	Keck	NIRC2	Kp	75.8	-557.7	-4.6	5.8	10.0	4.0	0.0
2004-07-11	09:04:38.59	Keck	NIRC2	Kp	-37.3	-605.2	-1.6	4.7	10.0	3.8	0.0
2004-07-11	09:06:17.61	Keck	NIRC2	Kp	-31.4	-594.0	3.5	15.7	10.0	3.2	0.0
2004-07-24	04:06:15.08	VLT	NACO	H	-102.4	494.0	-4.1	-8.3	13.3	4.1	0.0
2004-07-26	01:26:46.89	VLT	NACO	H	161.2	-436.9	3.0	5.3	13.3	4.1	0.0
2004-07-26	03:22:05.69	VLT	NACO	H	214.8	-384.2	9.8	0.6	13.3	6.6	0.2
2004-07-26	04:51:30.92	VLT	NACO	H	243.1	-333.7	4.5	1.4	13.3	5.0	0.1
2004-10-07	00:20:01.16	VLT	NACO	Ks	156.7	359.1	-1.2	-6.3	13.3	4.4	0.1
2004-10-07	00:30:14.12	VLT	NACO	Ks	151.2	357.4	-5.0	-10.7	13.3	4.9	0.1
2004-10-07	00:45:06.38	VLT	NACO	Ks	159.2	375.5	5.5	3.5	13.3	4.6	0.1
2005-05-31	14:59:17.38	Keck	NIRC2	Kp	-368.8	-216.9	-2.3	5.2	10.0	4.3	0.0
2006-12-12	13:42:00.42	Keck	NIRC2	Kp	124.4	-873.1	-15.9	-10.8	10.0	4.2	0.0
2008-01-21	11:36:28.68	Keck	NIRC2	Kp	57.2	579.7	-2.8	13.8	10.0	3.7	0.1
2008-01-21	11:43:51.91	Keck	NIRC2	Kp	48.9	572.6	-5.9	6.1	10.0	4.3	0.0
2008-01-21	12:31:09.49	Keck	NIRC2	Kp	11.2	572.4	-10.1	3.5	10.0	4.3	0.0
2008-01-21	13:12:50.82	Keck	NIRC2	Kp	-19.3	568.6	-10.9	-0.9	10.0	4.2	0.0
2008-01-21	13:54:28.00	Keck	NIRC2	Kp	-43.7	565.0	-5.8	-3.6	10.0	4.2	0.0
2008-01-21	14:55:05.79	Keck	NIRC2	Kp	-82.2	564.2	-1.4	-0.5	10.0	4.2	0.0
2008-01-21	15:57:45.30	Keck	NIRC2	Kp	-131.6	555.7	-6.9	-1.8	10.0	4.1	0.0
2008-01-21	16:06:05.01	Keck	NIRC2	Kp	-139.6	556.0	-9.1	-0.3	10.0	4.1	0.0
2009-06-07	11:34:45.65	Keck	NIRC2	K	191.1	634.3	-9.5	5.8	10.0	4.0	0.0
2010-06-28	12:44:51.55	Keck	NIRC2	FeII	567.3	-49.7	-6.1	-17.1	10.0	4.7	1.2
2010-08-26	12:25:53.86	Keck	NIRC2	Kp	-565.3	-307.4	-5.0	17.0	10.0	4.5	0.0
2010-08-26	13:22:31.41	Gemini	NIRI	Kp	-597.3	-268.7	-6.0	12.3	21.9	3.7	0.0
2010-08-26	13:33:09.44	Gemini	NIRI	Kp	-601.2	-262.2	-4.4	10.5	21.9	3.7	0.0
2010-08-30	06:42:20.85	VLT	NACO	Ks	-668.5	-120.8	2.2	7.4	13.3	4.4	0.0
2010-08-30	06:47:40.78	VLT	NACO	Ks	-668.6	-116.7	3.9	7.1	13.3	4.4	0.0
2010-08-30	06:52:58.60	VLT	NACO	Ks	-669.4	-115.6	5.0	3.7	13.3	4.3	0.1
2010-08-30	06:57:55.00	VLT	NACO	Ks	-675.6	-112.8	0.4	2.4	13.3	4.3	0.0

Table B.3: continued

Date	UTC	Tel.	Cam.	Filter	X_o (mas)	Y_o (mas)	X_{o-c} (mas)	Y_{o-c} (mas)	σ (mas)	ΔM (mag)	δM (mag)
2010-08-30	07:03:01.82	VLT	NACO	Ks	-677.5	-104.9	0.3	6.0	13.3	4.3	0.0
2010-08-30	07:09:26.05	VLT	NACO	Ks	-677.3	-99.5	2.6	6.0	13.3	4.3	0.0
2010-09-15	10:31:57.01	Gemini	NIRI	Kp	647.6	116.4	12.0	-9.7	21.9	3.7	0.0
2010-09-16	09:18:06.38	Gemini	NIRI	Kp	239.1	-699.6	-11.5	-2.5	21.9	3.6	0.0
2010-09-17	09:52:44.88	Gemini	NIRI	Kp	-703.6	102.7	-5.3	14.6	21.9	3.8	0.0
2010-10-30	07:15:04.22	Gemini	NIRI	Kp	-475.1	-173.9	-3.1	14.7	21.9	3.1	0.0
2010-10-30	08:22:28.80	Gemini	NIRI	Kp	-495.0	-128.5	2.2	11.6	21.9	3.5	0.1
2010-10-31	07:17:43.32	Gemini	NIRI	Kp	-230.8	613.2	11.1	4.5	21.9	3.6	0.0
2011-11-10	14:56:31.94	Keck	NIRC2	FeII	40.6	-639.7	-10.1	-11.9	10.0	4.2	0.0
2015-08-05	06:12:36.29	VLT	IRDIS	H	-255.5	-583.7	5.7	11.7	12.3	4.7	0.0
2015-08-06	08:50:19.71	VLT	IRDIS	H	-536.8	508.1	9.3	2.5	12.3	4.1	0.0
2015-08-06	08:55:55.18	VLT	IRDIS	H	-531.9	511.3	10.9	2.7	12.3	4.4	0.0
2015-08-06	09:03:38.30	VLT	IRDIS	H	-527.1	514.9	11.2	2.1	12.3	4.5	0.0
2015-08-22	07:32:01.75	VLT	IRDIS	H	712.2	-318.7	-6.7	-1.6	12.3	4.1	0.0
2015-08-25	04:45:18.09	VLT	IRDIS	H	450.0	481.0	-4.1	-14.6	12.3	3.7	0.0
2015-08-25	04:51:33.71	VLT	IRDIS	H	455.6	476.2	-3.2	-15.5	12.3	3.7	0.0
2015-08-28	06:19:53.45	VLT	IRDIS	H	-213.3	697.6	7.3	-6.8	12.3	3.8	0.0
2015-08-28	06:26:23.81	VLT	IRDIS	H	-208.0	699.2	6.7	-5.9	12.3	3.8	0.0
2015-09-06	03:38:54.27	VLT	IRDIS	H	334.6	-683.4	-1.2	5.1	12.3	3.4	0.0
2015-09-06	03:45:23.25	VLT	IRDIS	H	327.0	-681.3	-3.3	8.7	12.3	3.8	0.0
2015-09-06	03:51:39.55	VLT	IRDIS	H	322.4	-682.3	-2.6	9.1	12.3	3.8	0.0
2018-03-15	08:03:46.46	VLT	ZIMPOL	R	486.4	-512.0	7.1	-10.7	7.2	4.7	0.0
2018-03-15	08:28:25.25	VLT	ZIMPOL	R	501.0	-494.3	6.9	-6.8	7.2	4.6	0.0
2018-04-20	05:11:36.58	VLT	ZIMPOL	R	400.1	-549.6	0.1	-10.8	7.2	4.6	0.0
2018-04-20	05:36:16.45	VLT	ZIMPOL	R	416.3	-538.9	-0.3	-12.0	7.2	4.6	0.0
2018-05-04	23:30:43.20	VLT	ZIMPOL	R	640.4	-177.0	12.8	-5.6	7.2	4.1	0.0
2018-05-04	23:55:24.19	VLT	ZIMPOL	R	645.2	-155.1	12.2	-2.1	7.2	4.1	0.0
2018-05-05	02:34:13.23	VLT	ZIMPOL	R	656.0	-37.6	2.2	-5.1	7.2	4.1	0.0
2018-05-05	02:58:53.71	VLT	ZIMPOL	R	660.4	-19.8	5.6	-6.2	7.2	4.1	0.0
2019-06-09	08:50:43.39	VLT	ZIMPOL	R	-133.0	459.3	-5.7	-2.3	7.2	4.6	0.0
2019-06-09	09:08:08.97	VLT	ZIMPOL	R	-138.5	445.1	-6.5	-5.7	7.2	4.6	0.0
2019-06-27	03:38:22.22	VLT	ZIMPOL	R	-39.9	599.3	4.7	1.3	7.2	4.7	0.0
2019-06-27	03:55:48.28	VLT	ZIMPOL	R	-45.0	593.3	5.9	2.0	7.2	4.8	0.0
2019-07-08	00:30:49.73	VLT	ZIMPOL	R	-89.1	530.2	-1.4	-4.8	7.2	4.8	0.0
2019-07-08	00:48:15.01	VLT	ZIMPOL	R	-94.6	521.1	-0.4	-5.7	7.2	4.8	0.0
2021-12-30	20:15:00.00	C2PU	PISCO	V	58.0	-368.0	-21.3	13.0	8.1	–	–
2021-12-30	20:53:40.00	C2PU	PISCO	V	60.0	-425.0	-16.5	-7.0	7.8	3.9	0.3
2021-12-30	21:41:04.00	C2PU	PISCO	V	65.0	-456.0	-7.9	6.1	9.2	3.9	0.2
2021-12-30	22:18:43.00	C2PU	PISCO	V	47.0	-494.0	-22.8	1.9	10.8	–	–
2021-12-30	23:12:37.00	C2PU	PISCO	V	43.0	-553.0	-22.2	-10.4	5.8	3.4	0.2
2021-12-31	00:23:13.00	C2PU	PISCO	V	50.0	-585.0	-8.7	15.1	5.8	3.4	0.2
2021-12-31	01:13:00.00	C2PU	PISCO	V	48.0	-645.0	-5.8	-7.0	10.3	–	–
2021-12-31	01:43:00.00	C2PU	PISCO	V	49.0	-662.0	-1.8	-2.4	10.0	–	–
2021-12-31	02:10:00.00	C2PU	PISCO	V	42.0	-662.0	-6.0	16.4	20.6	–	–
2021-12-31	19:17:59.00	C2PU	PISCO	V	-63.0	-744.0	5.1	-1.7	5.8	3.5	0.4
2021-12-31	20:23:42.00	C2PU	PISCO	V	-69.0	-695.0	5.0	7.7	6.7	–	–
2021-12-31	20:48:33.00	C2PU	PISCO	V	-74.0	-674.0	2.1	12.5	5.8	3.6	0.2
2021-12-31	21:42:32.00	C2PU	PISCO	V	-74.0	-643.0	6.5	6.3	6.4	4.1	0.4
2021-12-31	22:36:33.00	C2PU	PISCO	V	-85.0	-601.0	-0.5	8.2	6.4	–	–
2021-12-31	23:30:31.00	C2PU	PISCO	V	-87.0	-556.0	1.3	10.7	6.7	–	–
2022-01-01	00:24:54.00	C2PU	PISCO	V	-70.0	-528.0	21.6	-6.7	13.6	3.7	0.2
2022-01-01	01:17:39.00	C2PU	PISCO	V	-91.0	-471.0	3.5	4.2	13.5	3.7	0.2
2022-01-01	02:11:38.00	C2PU	PISCO	V	103.0	-413.0	-5.8	13.1	8.6	–	–
2022-01-01	03:03:20.00	C2PU	PISCO	V	108.0	-399.0	-8.7	-21.7	5.4	–	–

Notes. Date, mid-observing time (UTC), telescope, camera, filter, astrometry (X is aligned with right ascension, and Y with declination, and the indices o and c stand for observed and computed positions), and photometry (magnitude difference ΔM with uncertainty δM).

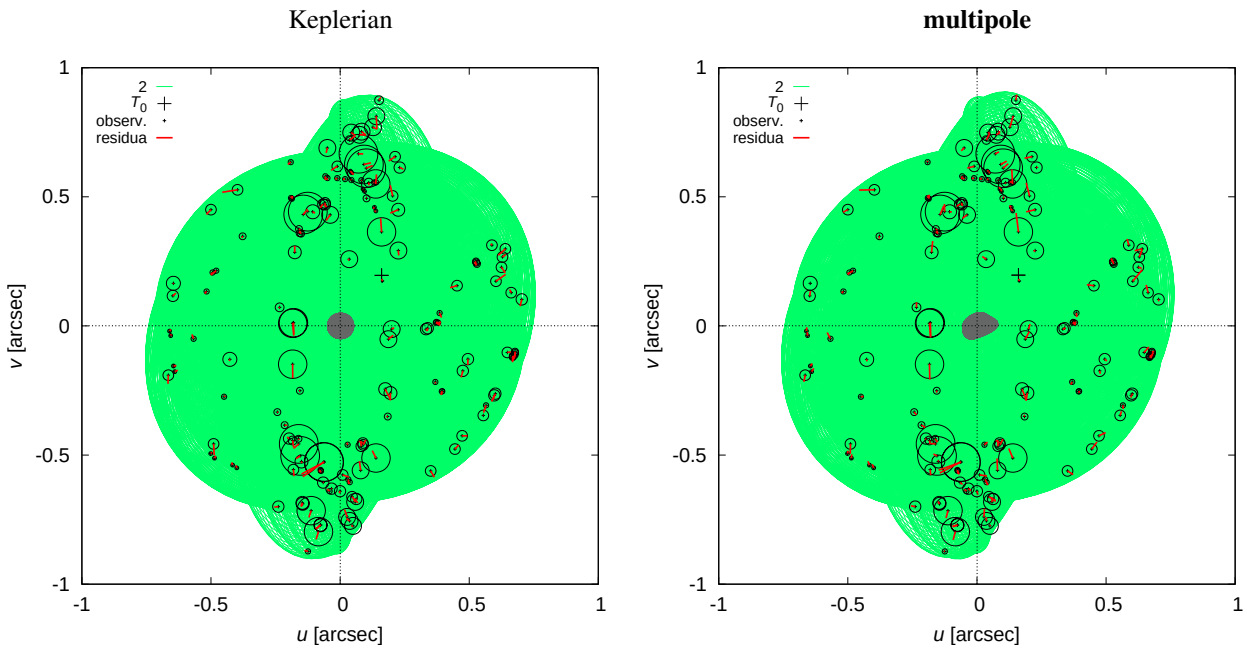

Fig. B.4: Sky-plane positions (u, v) and trajectories for two dynamical models: Keplerian (left) and multipole (right). Observed positions are plotted as black crosses and uncertainty ellipses, trajectories (with variable geometry) as green lines, and residuals as red lines. Both models are comparable in terms of $\chi^2_{\rm sky}$ (202 vs 226; see Table 2).

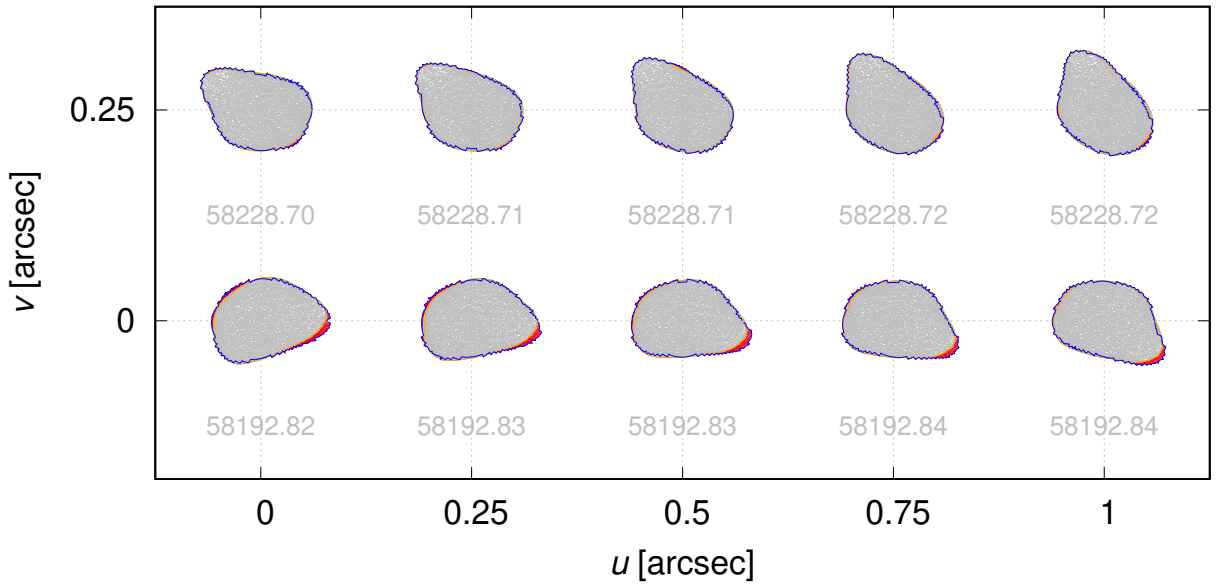

Fig. B.5: Residuals of AO silhouettes (in red) when using the best-fit pole l = 195.6°, b = 2.2°, according to the multipole model. The surface shape was adjusted for this pole. The value of $\chi^2_{\rm ao}$ = 443. A total of 35 silhouettes were used. Only the bottom row is affected by deconvolution artifacts due to fast rotation.

Table B.4: Multipole coefficients of Kalliope's gravitational field, using the ADAM model and constant density.

C_{00}	1.00000000		
C_{10}	0.00000000		
C_{11}	0.00000000	S_{11}	0.00000000
C_{20}	$-1.58875562 \cdot 10^{-1}$		
C_{21}	$-4.33435120 \cdot 10^{-3}$	S_{21}	$-2.42113162 \cdot 10^{-3}$
C_{22}	$4.73395888 \cdot 10^{-2}$	S_{22}	$3.38835106 \cdot 10^{-5}$
C_{30}	$1.16834450 \cdot 10^{-2}$		
C_{31}	$2.37513333 \cdot 10^{-2}$	S_{31}	$5.93605589 \cdot 10^{-3}$
C_{32}	$-2.04115124 \cdot 10^{-3}$	S_{32}	$-2.46015062 \cdot 10^{-3}$
C_{33}	$-7.49059459 \cdot 10^{-4}$	S_{33}	$-3.37228585 \cdot 10^{-3}$
C_{40}	$4.74784983 \cdot 10^{-2}$		
C_{41}	$-4.88209013 \cdot 10^{-3}$	S_{41}	$-3.28678691 \cdot 10^{-3}$
C_{42}	$-4.08073011 \cdot 10^{-3}$	S_{42}	$-1.03036986 \cdot 10^{-3}$
C_{43}	$1.31697945 \cdot 10^{-4}$	S_{43}	$1.86676711 \cdot 10^{-4}$
C_{44}	$2.78751167 \cdot 10^{-4}$	S_{44}	$2.77201832 \cdot 10^{-4}$
C_{50}	$-1.75298664 \cdot 10^{-2}$		
C_{51}	$-1.71149768 \cdot 10^{-2}$	S_{51}	$-4.31000895 \cdot 10^{-3}$
C_{52}	$1.11174185 \cdot 10^{-3}$	S_{52}	$8.17553521 \cdot 10^{-4}$
C_{53}	$4.23873557 \cdot 10^{-4}$	S_{53}	$4.82680368 \cdot 10^{-4}$
C_{54}	$-4.05737556 \cdot 10^{-5}$	S_{54}	$-5.48759157 \cdot 10^{-5}$
C_{55}	$-8.11236571 \cdot 10^{-6}$	S_{55}	$-5.34460804 \cdot 10^{-5}$
C_{60}	$-2.26407423 \cdot 10^{-2}$		
C_{61}	$1.06155467 \cdot 10^{-2}$	S_{61}	$3.17450599 \cdot 10^{-3}$
C_{62}	$8.94341691 \cdot 10^{-4}$	S_{62}	$9.19312511 \cdot 10^{-4}$
C_{63}	$-1.61567819 \cdot 10^{-4}$	S_{63}	$-1.67419911 \cdot 10^{-4}$
C_{64}	$-8.84803606 \cdot 10^{-6}$	S_{64}	$-4.37031557 \cdot 10^{-5}$
C_{65}	$7.37179627 \cdot 10^{-7}$	S_{65}	$5.61944021 \cdot 10^{-6}$
C_{66}	$-4.17890001 \cdot 10^{-7}$	S_{66}	$3.62295627 \cdot 10^{-6}$
C_{70}	$3.54897487 \cdot 10^{-2}$		
C_{71}	$-2.69712613 \cdot 10^{-2}$	S_{71}	$5.68137067 \cdot 10^{-4}$
C_{72}	$-1.08514637 \cdot 10^{-3}$	S_{72}	$-6.51499801 \cdot 10^{-4}$
C_{73}	$-1.46230432 \cdot 10^{-4}$	S_{73}	$-1.42955377 \cdot 10^{-4}$
C_{74}	$1.22190952 \cdot 10^{-5}$	S_{74}	$1.96896452 \cdot 10^{-5}$
C_{75}	$1.48302902 \cdot 10^{-6}$	S_{75}	$5.23611262 \cdot 10^{-6}$
C_{76}	$-1.01335926 \cdot 10^{-7}$	S_{76}	$-5.49383918 \cdot 10^{-7}$
C_{77}	$8.59087060 \cdot 10^{-8}$	S_{77}	$-3.07710303 \cdot 10^{-7}$
C_{80}	$2.06218064 \cdot 10^{-2}$		
C_{81}	$-1.44307265 \cdot 10^{-2}$	S_{81}	$-3.51810426 \cdot 10^{-3}$
C_{82}	$-4.64071911 \cdot 10^{-4}$	S_{82}	$-6.73665797 \cdot 10^{-4}$
C_{83}	$1.41998313 \cdot 10^{-4}$	S_{83}	$1.23775069 \cdot 10^{-4}$
C_{84}	$8.48390705 \cdot 10^{-7}$	S_{84}	$1.62927728 \cdot 10^{-5}$
C_{85}	$-8.08521429 \cdot 10^{-7}$	S_{85}	$-2.56842858 \cdot 10^{-6}$
C_{86}	$1.50086522 \cdot 10^{-7}$	S_{86}	$-3.68754057 \cdot 10^{-7}$
C_{87}	$-1.24729943 \cdot 10^{-8}$	S_{87}	$5.30096051 \cdot 10^{-8}$
C_{88}	$-1.40328492 \cdot 10^{-8}$	S_{88}	$1.73822097 \cdot 10^{-8}$
C_{90}	$-7.38068869 \cdot 10^{-2}$		
C_{91}	$-4.31387796 \cdot 10^{-3}$	S_{91}	$-1.97973583 \cdot 10^{-3}$
C_{92}	$1.04198061 \cdot 10^{-3}$	S_{92}	$5.14153229 \cdot 10^{-4}$
C_{93}	$-1.35824568 \cdot 10^{-4}$	S_{93}	$5.18308966 \cdot 10^{-4}$
C_{94}	$-8.06877944 \cdot 10^{-6}$	S_{94}	$-1.41329178 \cdot 10^{-5}$
C_{95}	$-2.35844582 \cdot 10^{-8}$	S_{95}	$-1.11646481 \cdot 10^{-6}$
C_{96}	$-7.20088131 \cdot 10^{-11}$	S_{96}	$1.98019520 \cdot 10^{-7}$
C_{97}	$-9.46264001 \cdot 10^{-9}$	S_{97}	$2.27384973 \cdot 10^{-8}$
C_{98}	$1.53136052 \cdot 10^{-9}$	S_{98}	$-3.04644339 \cdot 10^{-9}$
C_{99}	$1.08668869 \cdot 10^{-9}$	S_{99}	$-8.38316486 \cdot 10^{-10}$
$C_{10,0}$	$-1.52754324 \cdot 10^{-2}$		
$C_{10,1}$	$1.68702648 \cdot 10^{-2}$	$S_{10,1}$	$4.00489156 \cdot 10^{-3}$
$C_{10,2}$	$2.19255958 \cdot 10^{-4}$	$S_{10,2}$	$3.84832391 \cdot 10^{-4}$
$C_{10,3}$	$-1.22227813 \cdot 10^{-4}$	$S_{10,3}$	$-1.09283485 \cdot 10^{-4}$
$C_{10,4}$	$1.14264963 \cdot 10^{-7}$	$S_{10,4}$	$-6.19634189 \cdot 10^{-6}$
$C_{10,5}$	$4.66051178 \cdot 10^{-7}$	$S_{10,5}$	$1.41886391 \cdot 10^{-6}$
$C_{10,6}$	$-4.23016143 \cdot 10^{-8}$	$S_{10,6}$	$8.23703808 \cdot 10^{-8}$
$C_{10,7}$	$2.98805253 \cdot 10^{-9}$	$S_{10,7}$	$-1.64044820 \cdot 10^{-8}$
$C_{10,8}$	$1.40038401 \cdot 10^{-9}$	$S_{10,8}$	$-1.16432341 \cdot 10^{-9}$
$C_{10,9}$	$-1.58497488 \cdot 10^{-10}$	$S_{10,9}$	$2.06969430 \cdot 10^{-10}$
$C_{10,10}$	$-8.00938275 \cdot 10^{-11}$	$S_{10,10}$	$3.06719370 \cdot 10^{-11}$

Notes. The normalization is given by Eq. (A.1). The reference radius is $R = 76.411$ km.